

Aerodynamic Shape Optimization of an Adaptive Morphing Trailing Edge Wing

Zhoujie Lyu¹

Joaquim R. R. A. Martins²

Department of Aerospace Engineering, University of Michigan, Ann Arbor, MI

Abstract Adaptive morphing trailing edge wings have the potential to reduce the fuel burn of transport aircraft. However, to take full advantage of this technology and to quantify its benefits, design studies are required. To address this need, we quantify the aerodynamic performance benefits of a morphing trailing edge wing using aerodynamic design optimization. The aerodynamic model solves the Reynolds-averaged Navier–Stokes equations with a Spalart–Allmaras turbulence model. A gradient-based optimization algorithm is used in conjunction with an adjoint method that computes the required derivatives. The baseline geometry is optimized using a multipoint formulation and 192 shape design variables. The average drag coefficient is minimized subject to lift, pitching moment, geometric constraints, and a 2.5 g maneuver bending moment constraint. The trailing edge of the wing is optimized based on the multipoint optimized wing. The trailing edge morphing is parameterized using 90 design variables that are optimized independently for each flight condition. A total of 407 trailing edge optimizations are performed at different flight conditions to span the entire flight envelope. We observed 1% drag reduction at on-design conditions, and 5% drag reduction near off-design conditions. The effectiveness of the trailing edge morphing is demonstrated by comparing it with the optimized results of a hypothetical fully morphing wing. In addition, we compute the fuel-burn reductions for a number of flights using the optimization results. A 1% cruise fuel-burn reduction is achieved using an adaptive morphing trailing edge for a typical long-haul twin-aisle mission.

1 Introduction

Given the rise in environmental concerns and the volatility in fuel prices, airlines and aircraft manufacturers alike are seeking more efficient aircraft. Research in aircraft design is therefore placing an increasing emphasis on fuel-burn reduction. One of the fuel-burn reduction strategies that is currently used on modern jetliners, such as the Boeing 787, is the use of cruise flaps, where a small amount of trailing edge (TE) flap and aileron droop is used to optimize the aerodynamic performance at different cruise conditions. While cruise flaps do reduce the drag, they have a limited number of degrees of freedom. Morphing TE devices, such as FlexSys FlexFoil, could address this issue by changing the camber and flap angles at each spanwise location using a smooth morphing surface with no gaps [1, 2]. The morphing TE has a high level of technology readiness and has the potential to be retrofitted onto existing aircraft to reduce the drag as much as possible for each flight condition.

Previous studies on the morphing TE have focused on the design of the morphing mechanism, the actuators, and the structure [1, 2, 3]. In previous aerodynamic studies of the morphing TE, low-fidelity methods were used [4, 5]. However, small geometry changes, such as the cruise-flap extension, require high-fidelity simulations to fully quantify the tradeoff between the induced drag and other sources of drag. In this paper, we use a high-fidelity aerodynamic model based on the Reynolds-averaged Navier–Stokes (RANS) equations to examine this tradeoff. The boundary layer is well resolved and a Spalart–Allmaras turbulence model is used.

We performed a multipoint aerodynamic shape optimization of the wing to provide an optimized baseline to evaluate the TE optimization. The determination of the optimal TE shape at each spanwise location for each flight condition is a challenging design task. We use a gradient-based numerical optimization

algorithm together with an efficient adjoint implementation [6] to optimize the morphing for the different flight conditions. A database of optimal morphing shapes at different flight conditions is generated using a total of 407 aerodynamic shape optimizations. Once the database has been generated, we can compute the required optimal morphing shapes and related fuel-burn reductions for each mission. For comparison purposes, we also perform the design optimization of a fully morphing wing to quantify the theoretical minimal drag for each condition.

This paper is organized as follows. Section 2 discusses the computational tools used in this study, and Section 3 gives the baseline geometry and optimization problem formulations. We perform a multipoint optimization of the wing in Section 4 and present the morphing TE optimization results in Section 5. We then discuss the fully morphing wing optimization and compare it to the morphing TE results in Sections 6 and 7. We simulate a number of flight missions and quantify the fuel-burn reduction with the adaptive morphing TE in Section 8.

2 Computational Tools

This section describes the numerical tools and methods that are used for the shape optimization studies. These tools are components of the framework for the multidisciplinary design optimization (MDO) of aircraft configurations with high fidelity (MACH) [7]. MACH can perform the simultaneous optimization of aerodynamic shape and structural sizing variables considering aeroelastic deflections [8]. However, in this paper we use only the components of MACH that are relevant for aerodynamic shape optimization: the geometric parametrization, mesh perturbation, CFD solver, and optimization algorithm. This setup has been successfully used to study aerodynamic design optimization problems [9, 10, 11, 12].

2.1 Geometric Parametrization

We use a free-form deformation (FFD) approach to parametrize the geometry [13]. The FFD volume parametrizes the geometry changes rather than the geometry itself, resulting in a more efficient and compact set of geometry design variables, and thus making it easier to handle complex geometric manipulations. We may embed any geometry inside the volume by performing a Newton search to map the parameter space to physical space. All the geometric changes are performed on the outer boundary of the FFD volume. Any modification of this outer boundary indirectly modifies the embedded objects. The key assumption of the FFD approach is that the geometry has constant topology throughout the optimization process, which is usually the case for wing design. In addition, since FFD volumes are trivariate B-spline volumes, the sensitivity information of any point inside the volume can easily be computed. Figure 1 shows the FFD volume and geometric control points for the aerodynamic shape optimization.

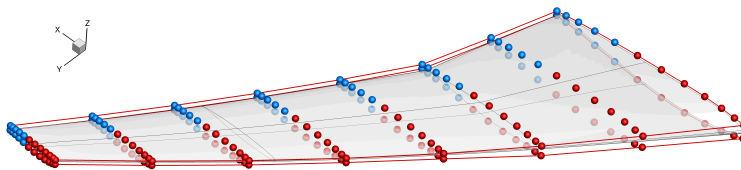


Figure 1: The wing shape design variables are the z -displacement of 192 FFD control points (red and blue spheres). The TE morphing design variables are the blue control points.

To simulate the TE morphing, the last five chordwise top-bottom pairs of control points (shown in blue in Fig. 1) can move independently in the z direction. This results in a smooth morphing of the rear 45% of the chord that can tailor the airfoil camber in the spanwise direction for each flight condition. This simulates a morphing TE similar to that of the FlexSys morphing wing [2]. Because of the constant topology assumption of the FFD approach, and due to limitations in the mesh perturbation, the surface has to be continuous around the control surfaces, eliminating the control surface gap. Therefore, when the control surfaces deflect, there is a transition region between the control surface and the centerbody, similar to that studied in a continuous morphing wing [2].

2.2 Mesh Perturbation

Since FFD volumes modify the geometry during the optimization, we must perturb the mesh for the CFD analysis to solve for the modified geometry. The mesh perturbation scheme used in this work is a hybridization of algebraic and linear elasticity methods [13]. The idea behind the hybrid warping scheme is to apply a linear-elasticity-based warping scheme to a coarse approximation of the mesh to account for large low-frequency perturbations, and to use the algebraic warping approach to attenuate small high-frequency perturbations. The goal is to compute a high-quality perturbed mesh similar to that obtained using a linear elasticity scheme, but at a much lower computational cost.

2.3 CFD Solver

We use the S Umb flow solver [14]. S Umb is a finite-volume, cell-centered multiblock solver for the compressible Euler, laminar Navier–Stokes, and RANS equations (steady, unsteady, and time-periodic). It provides options for a variety of turbulence models with one, two, or four equations and options for adaptive wall functions. The Jameson–Schmidt–Tukel (JST) scheme [15] augmented with artificial dissipation is used for the spatial discretization. The main flow is solved using an explicit multi-stage Runge–Kutta method along with a geometric multi-grid scheme. A segregated Spalart–Allmaras (SA) turbulence equation is iterated with the diagonally dominant alternating direction implicit (DDADI) method. An automatic differentiation adjoint for the Euler and RANS equations has been developed to compute the gradients [6, 16]. The adjoint implementation supports both the full-turbulence and frozen-turbulence modes, but in the present work we use the full-turbulence adjoint exclusively. The adjoint equations are solved with the preconditioned generalized minimal residual method (GMRES) [17] using the Portable, Extensible Toolkit for Scientific Computation (PETSc) [18, 19, 20].

2.4 Optimization Algorithm

Because of the high computational cost of CFD solutions, it is critical to choose an optimization algorithm that requires a reasonably low number of function evaluations. Given the large numbers of variables required for aerodynamic shape optimization, our only feasible option is to use a gradient-based optimizer. While this type of optimizer converges to a single local minimum, we have previously established that for this type of problem, there are no significant multiple local minima. Most of the design space seems to be convex, with a single region that has closely spaced multiple local minima, for which the differences in the drag coefficients are less than 0.05% [10]. For these reasons, we use a gradient-based optimizer combined with adjoint gradient evaluations to solve the problem efficiently.

The optimization algorithm used for all results presented herein is SNOPT (sparse nonlinear optimizer) [21] through the Python interface pyOpt [22]. SNOPT is a gradient-based optimizer that implements a sequential quadratic programming method; it is capable of solving large-scale nonlinear optimization problems with thousands of constraints and design variables. SNOPT uses a smooth augmented Lagrangian merit function, and the Hessian of the Lagrangian is approximated using a limited-memory quasi-Newton method.

3 Optimization Problem Formulation

All the optimizations perform lift-constrained drag minimization of the wing using the RANS equations. In this section, we provide a complete description of the problems. This type of optimization problem formulation has been previously used by the authors [10].

3.1 Common Research Model Wing

The initial geometry is a wing with a blunt TE extracted from the NASA Common Research Model (CRM) wing-body geometry, which is representative of a contemporary transonic commercial transport [23, 24], with a size similar to that of a Boeing 777. Several design features, such as an aggressive pressure recovery in the outboard wing, were introduced into the design to make it more interesting for research purposes and to protect intellectual property. This initial geometry provides a reasonable starting point for the optimization, while leaving room for further performance improvements. In addition, the CRM was designed together with the fuselage of the complete CRM configuration, so its performance is degraded when only the wing is considered.

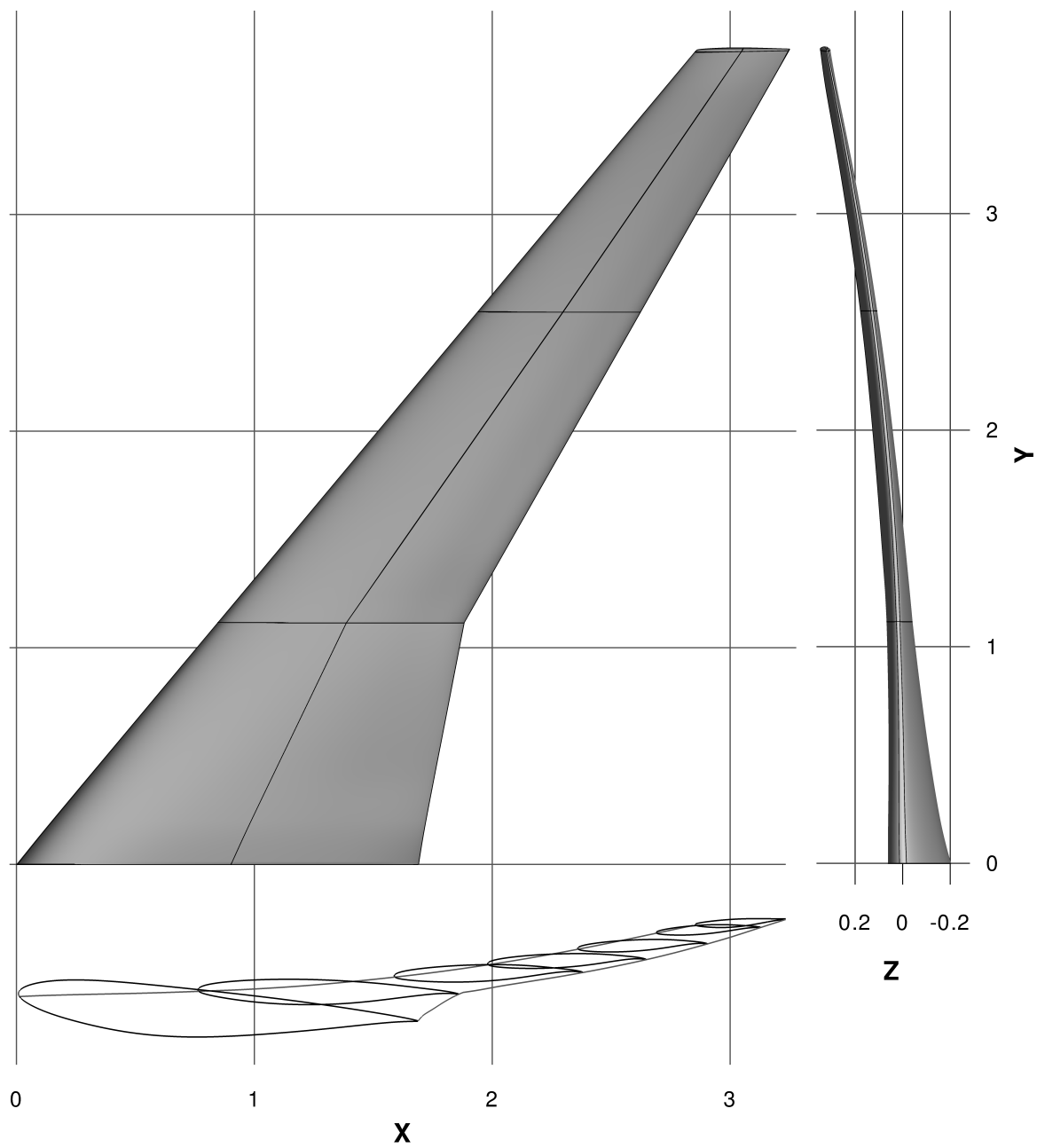


Figure 2: CRM wing geometry scaled by its mean aerodynamic chord.

The geometry and specifications for this wing are given by the Aerodynamic Design Optimization Discussion Group (ADODG)¹ and were used as the basis for a benchmark single-point aerodynamic shape optimization problem defined by the group [10]. The CRM wing geometry is shown in Fig. 2. All the coordinates are scaled by the mean aerodynamic chord (275.8 in). The resulting reference chord is 1.0, and the half span is 3.758151. The pitching moment reference point is at $x = 1.2077$ and $z = 0.007669$, and the reference area is 3.407014 [10].

3.2 Volume Grid

We generate the mesh for the CRM wing using an in-house hyperbolic mesh generator. The mesh is marched out from the surface mesh using an O-grid topology to a farfield located at a distance of 25 times the span (about 185 mean chords). The nominal cruise flow condition is Mach 0.85, with a Reynolds number of 5 million based on the mean aerodynamic chord. This Reynolds number is that specified by the CRM case and corresponds to the wind tunnel test. We used this value so that the results are comparable to the existing benchmarks. The mesh size and the flow solution values at the nominal operating condition are listed in Table 1. They are the same as those used by the authors to solve the ADODG CRM single-point benchmark problem, for which the meshes and geometries are publicly available [10].

Mesh level	Mesh size	C_D	C_L	C_M	α
$h = 0$	∞	0.01990			
L00	230,686,720	0.01992	0.5000	-0.1776	2.2199°
L0	28,835,840	0.01997	0.5000	-0.1790	2.2100°
L1	3,604,480	0.02017	0.5000	-0.1810	2.1837°
L2	450,560	0.02111	0.5000	-0.1822	2.1944°

Table 1: Mesh convergence study for the CRM wing [10].

We perform a mesh convergence study to determine the resolution accuracy of this mesh. Table 1 lists the drag and pitching moment coefficients for the initial meshes. We also compute the zero-grid spacing drag using Richardson’s extrapolation, which estimates the drag value as the grid spacing approaches zero [25]. The zero-grid spacing drag coefficient is 199.0 counts for the CRM wing. Since we need to perform hundreds of optimizations to optimize the TE for each flight condition, we use the L2 mesh to achieve a reasonable computational cost with sufficient accuracy. For simplicity, we use only the L2 mesh for the studies in this paper. However, a multilevel approach could be used to optimize a larger grid size [11].

3.3 Objective Function

The baseline multipoint aerodynamic shape optimization seeks to minimize the average drag coefficients (computed by RANS solutions) of five flight conditions by varying the shape design variables subject to constraints on the lift, pitching moment, and maneuver bending moment. Table 2 lists the lift coefficients and Mach numbers for the five aerodynamic performance flight conditions considered (1–5). The bending moment constraint is enforced at flight condition 6 (also computed with RANS), which corresponds to a 2.5 g pull-up maneuver. A similar multipoint approach has previously been presented by the authors [10]. The morphing optimizations use exactly the same objective and constraints, but the difference is that the TE can be optimized for each flight condition independently.

3.4 Design Variables

Before studying the TE morphing, we performed a multipoint aerodynamic shape optimization of the wing to obtain an optimized aerodynamic performance of the wing itself. The first set of design variables consists of control points distributed on the FFD volume. A total of 192 shape variables are distributed on the lower and upper surfaces of the FFD volume, as shown in Fig. 1. The large number of shape variables provides more degrees of freedom for the optimizer to explore, and this allows us to fine-tune the sectional airfoil shapes and the thickness-to-chord ratios at each spanwise location. Because of the efficient adjoint implementation, the cost of computing the shape gradients is nearly independent of the number of shape variables [7]. The fully morphing wing optimization uses the same set of shape design variables.

Flight condition	C_L	Mach number
1	0.50	0.85
2	0.55	0.85
3	0.45	0.85
4	0.50	0.84
5	0.50	0.86
6	2.5 g	0.86

Table 2: The multiple flight conditions represent a five-point stencil in Mach- C_L space and a 2.5 g maneuver case.

For the morphing TE optimization, we use a subset of the shape control points near the TE as the design variables, as shown in blue in Figure 1. Each point on the top surface is paired with a corresponding point on the bottom surface, and the z distance between each pair is constrained to be constant, i.e., the local thickness of the airfoil cannot be changed by the morphing mechanism. Only the shape over the last 45% of the chord is allowed to change. The shape of the forward wing remains constant.

3.5 Constraints

Since optimizers tend to exploit any weaknesses in numerical models and problem formulations, an optimization problem needs to be carefully constrained in order to yield a physically feasible design. We performed a multipoint optimization with 6 flight conditions: 5 cruise conditions and a 2.5 g maneuver condition. Both the lift and the pitching moment are constrained at the nominal flight condition (Mach 0.85, $C_L = 0.5$). The lift coefficient and pitching moment constraints are as defined in the ADODG case. The pitching moment coefficient would be trimmed to zero by the horizontal tail in a complete configuration. In addition, the wing root bending moment at the 2.5 g maneuver condition is constrained to be less than or equal to the nominal value, which is the bending moment of the baseline wing for the same maneuver condition. We also enforce several geometric constraints. First, we impose constant-thickness constraints distributed in a regular 25×30 grid: 25 points chordwise from the 1% to the 99% chord, at 30 spanwise stations from the root to the tip of the wing, resulting in a total of 750 thickness constraints. The lower bounds of these constraints are the baseline thicknesses at the corresponding locations, with no upper bound. These constraints ensure that the wing is practical from the structural point of view and that it can accommodate the high-lift system. The total volume of the wing is also constrained to meet a fuel-volume requirement. The complete optimization problem is described in Table 3.

	Function/variable	Description	Quantity
minimize	C_D	Drag coefficient	
with respect to	α	Angle of attack	1
	z	FFD control point z -coordinates	192
		Total design variables	193
subject to	$C_L = C_{L_{\text{target}}}$	Lift coefficient constraint	6
	$C_{M_y} \geq -0.17$	Pitching moment coefficient constraint	1
	$C_{\text{bend}} \leq C_{\text{bend}_{\text{base}}}$	Bending moment coefficient constraint	1
	$t \geq t_{\text{base}}$	Minimum thickness constraints	750
	$V \geq V_{\text{base}}$	Minimum volume constraint	1
		Total constraints	759

Table 3: Baseline aerodynamic shape optimization problem statement

4 Baseline Multipoint-Optimized Wing

Before we perform any morphing wing optimizations, we first optimize a fixed wing using a multipoint formulation to achieve a fair baseline for comparison that represents a wing that performs well at different flight conditions. Another reason for creating this baseline wing is that we are considering the wing alone, while the CRM wing was designed to perform well in the presence of the fuselage. In this section, we present our aerodynamic design optimization results for the baseline wing (described in Table 3), which considers five performance flight conditions and a 2.5 g maneuver condition. We use the L2 grid (450 k cells) for this optimization. Transport aircraft operate at multiple cruise conditions because of variability in the flight missions and air traffic control restrictions. Single-point optimization at the nominal cruise condition could overstate the benefit of the optimization, since the optimization improves the on-design performance to the detriment of the off-design performance. The single-point optimization benchmark problem developed by the ADODG resulted in an optimal wing with an unrealistically sharp leading edge in the outboard section of the wing [10]. This was caused by a combination of the low value for the thickness constraints (25% of the baseline) and the single-point formulation. Therefore, in this study, we use a multipoint formulation and 100% thickness constraints, which we have found to result in more realistic wings [10].

We choose five equally weighted flight conditions with different combinations of lift coefficient and Mach number, as previously done by the authors [26, 10]. The flight conditions are the nominal cruise, $\pm 10\%$ of cruise C_L , and ± 0.01 of cruise Mach, as shown in Table 2. More sophisticated ways of choosing the multipoint flight conditions and their associated weights could be used, such as the automated procedure developed by Liem *et al.* [27] that minimizes fleet-level fuel burn. The objective function is the average drag coefficient for the five flight conditions, and the pitching moment constraint is enforced only for the nominal flight condition. The bending moment constraint is enforced at the 2.5 g maneuver condition at 15,000 ft and Mach 0.86.

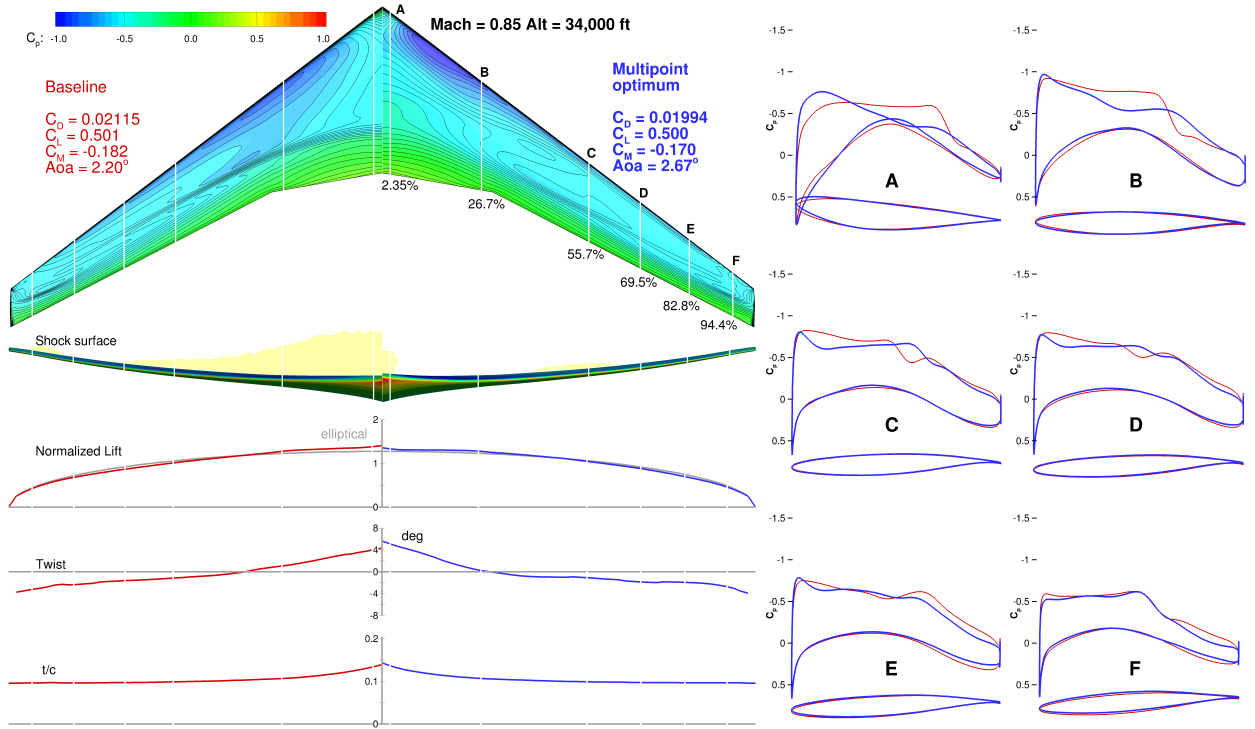


Figure 3: The multipoint optimized wing has 5.7% lower drag.

A comparison of the initial wing—the CRM wing—and the multipoint optimized design is shown in Fig. 3. The baseline results are shown in red (left wing), and the multipoint results are shown in blue (right wing); the lift, drag, and pitching moment coefficients are also listed. The C_p for the multipoint optimized result corresponds to the nominal condition (Mach 0.85, $C_L = 0.5$). We compute the shock surface from

the volume solution grid by constructing an isosurface of the normal Mach number [28]. The shock occurs where the normal Mach number is one, i.e.,

$$M_n = \frac{\vec{u}}{a} \cdot \frac{\nabla p}{|\nabla p|} = 1. \quad (1)$$

Unlike the shock-free design obtained with single-point optimization [10], the multipoint optimization settled on an optimal compromise between the flight conditions, resulting in a weak shock at all conditions. Similar trends were observed in the multipoint optimization of Vassberg and Jameson [29]. Our optimization procedure reduced the drag from 211.5 counts to 199.4 counts, a 5.7% reduction. At the optimum, the lift coefficient target is met, and the pitching moment is reduced to the lowest allowed value. The 2.5 g bending moment constraint is satisfied. The lift distribution of the optimized wing is much closer to the elliptical distribution than that of the baseline, indicating an induced drag that is close to the theoretical minimum for planar wakes. This is achieved by fine-tuning the twist distribution and airfoil shapes. The baseline wing has a near-linear twist distribution. The optimized design has more twist at the root and tip, and less twist near mid-wing. This multipoint optimized wing provides an initial geometry for the morphing TE and the fully morphing optimizations, as well as a baseline for performance comparisons.

5 Morphing Trailing Edge Wing Optimization

We perform a series of RANS-based aerodynamic shape optimizations to examine the effects of TE morphing. A gradient-based optimizer is used with derivatives computed via an adjoint method. The full-turbulence adjoint used includes the linearization of both the main flow solver and the SA turbulence model [6]. The optimizations are converged to an optimality tolerance of $\mathcal{O}(10^{-5})$. We use the optimized baseline geometry from Section 4 as the initial design point for the morphing TE optimization.

The shape aft of the 45% chord is free to change independently for each flight condition. The airfoil thickness is kept constant by the thickness constraints. A total of 80 design variables are used for each optimization. The angle-of-attack is also allowed to change during the optimization. To span the entire flight envelope, we performed 407 separate optimizations at various altitudes, Mach numbers, and weights. Each optimization required about 4 hours on 64 processors, corresponding to about 50 optimization iterations. No additional moment constraints are imposed in the optimization. Since the TE can be morphed independently for each flight condition, the 2.5 g maneuver bending moment constraint is easily satisfied using the morphing TE, and thus this constraint does not affect the optimal cruise morphing. The pitching moment constraint is still enforced only at the nominal flight condition, so trim drag is not accounted for at off-design conditions. Figures 4 to 7 show the TE optimization results for several on- and off-design conditions. Results for additional flight conditions are shown in Appendix A (Figs. 13 to 26).

At on-design conditions, the drag reductions range from 1% to 2%. The optimized TE shapes are close to the initial shape. However, we see that the optimizer is able to further smooth out the flow by introducing a slight camber at the TE. The TE deflection is less than 1 degree (measured from LE). The shock strength is reduced, illustrating that the transonic flow is sensitive to even slight changes in the TE shape. Similar trends are observed for several different weights.

At the off-design conditions, the difference between the optimized TE shape and the initial TE shape is more apparent. The maximum TE deflection at off-design conditions is about 3 degrees. The drag reduction due to the morphing TE is more significant, reaching 5%. At some extreme off-design cases, the flow is separated without a morphing TE. By optimizing the TE camber and shape, we reduce the angle-of-attack and re-attach the flow, significantly reducing the drag. The 2.5 g maneuver bending moment constraint is satisfied using the TE morphing. We conclude that the drag at all flight conditions can be reduced using the morphing TE, and that the benefit of a morphing TE is more significant for off-design conditions.

6 Fully Morphing Wing Optimization

We also performed a shape optimization assuming a fully morphing wing. Some technologies may one day achieve such large morphing [30, 31], so we are interested in finding out by how much the performance would increase relative to the morphing TE. We used a total of 192 shape design variables (the same set used for the baseline optimization) to optimize the entire wing at each flight condition. The rest of the optimization problem is the same as in Section 5. Similarly to the TE optimization, we performed 407

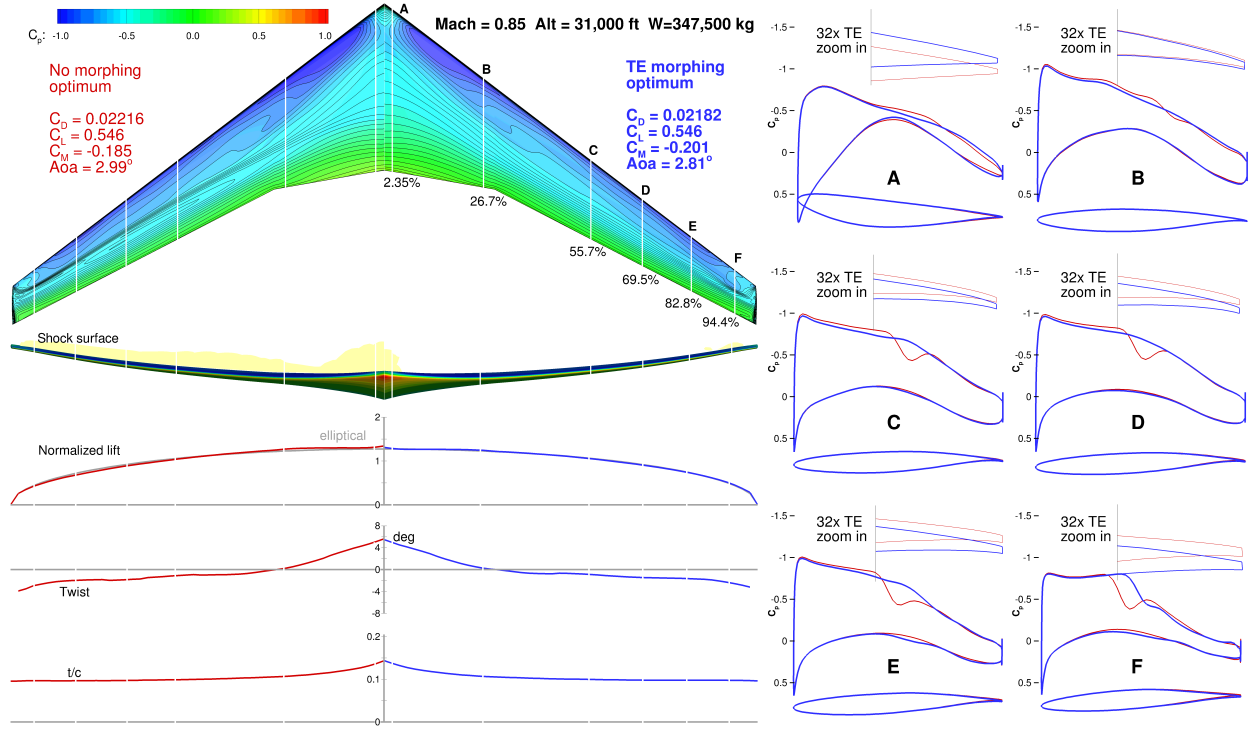


Figure 4: Morphing TE optimization at MTOW on-design condition.

separate optimizations for different altitudes, Mach numbers, and weights, to span the entire flight envelope. Because of the increased design-space dimensionality, the computational cost of the optimization is higher: 6 hours on 64 processors instead of 4 hours in the morphing TE case. Figures 8 and 9 show the fully morphing wing optimization results for an on-design and an off-design condition.

At on-design conditions, the fully morphing wing is only marginally better than the morphing TE wing. Specifically, the drag coefficient is decreased by about 1 count, as we can see by comparing the C_D values of the morphing TE wing in Fig. 4 and the fully morphing wing in Fig. 8. The baseline wing is already optimized near the cruise conditions; an additional drag reduction is difficult to achieve even with a fully morphing wing. The optimized wing shapes are very close to the baseline shape. The pressure distributions are also quite similar to those of the optimized morphing TE designs. Therefore, we see that it suffices to change the TE shape for drag reduction at on-design conditions.

At the off-design conditions, and similarly to the morphing TE, the fully morphing wing achieved an additional drag reduction of more than 5%. The maximum TE deflection at off-design conditions is about 3 degrees. In the flight condition shown in Fig. 9, the flow on the baseline wing is separated. The fully morphing wing still maintains a shock-free solution and near-elliptical lift distribution even at high C_L . We observe that the benefit of morphing wings can be magnified at off-design conditions.

7 Comparison Between Morphing Trailing Edge and Fully Morphing Wings

To further compare the benefits of the morphing TE and the morphing wing, we plotted the percentage drag reduction contours of each approach for the entire flight envelope for MTOW (347,500 kg), as shown in Figure 10. The drag reduction contours for other weights are shown in Appendix B (Figs. 27 and 28). The weight and altitude range is based on the Boeing 777-200LR operation manual for long-range cruise (LRC).

The trends of the two drag reduction contours are similar. The lowest drag reductions are near the on-design conditions where the wing has been previously optimized with a multipoint formulation. These drag reductions are due to the additional degrees of freedom that allow the TE shape to change separately at each flight condition, and they are also a result of making the 2.5g maneuver condition constraint independent through load alleviation with the morphing TE. At the lower Mach number range, the drag reduction increases with the altitude and Mach number. The highest drag reduction occurs at the flight condition with

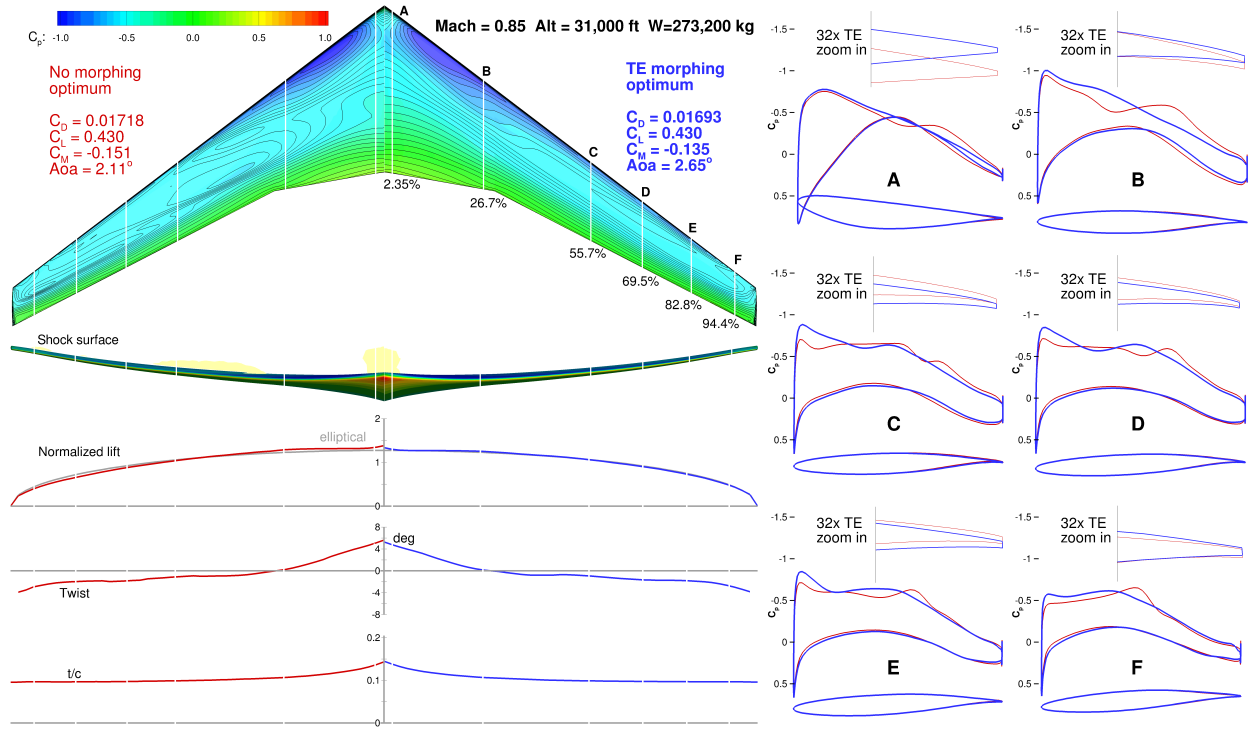


Figure 5: Morphing TE optimization at half-weight on-design condition.

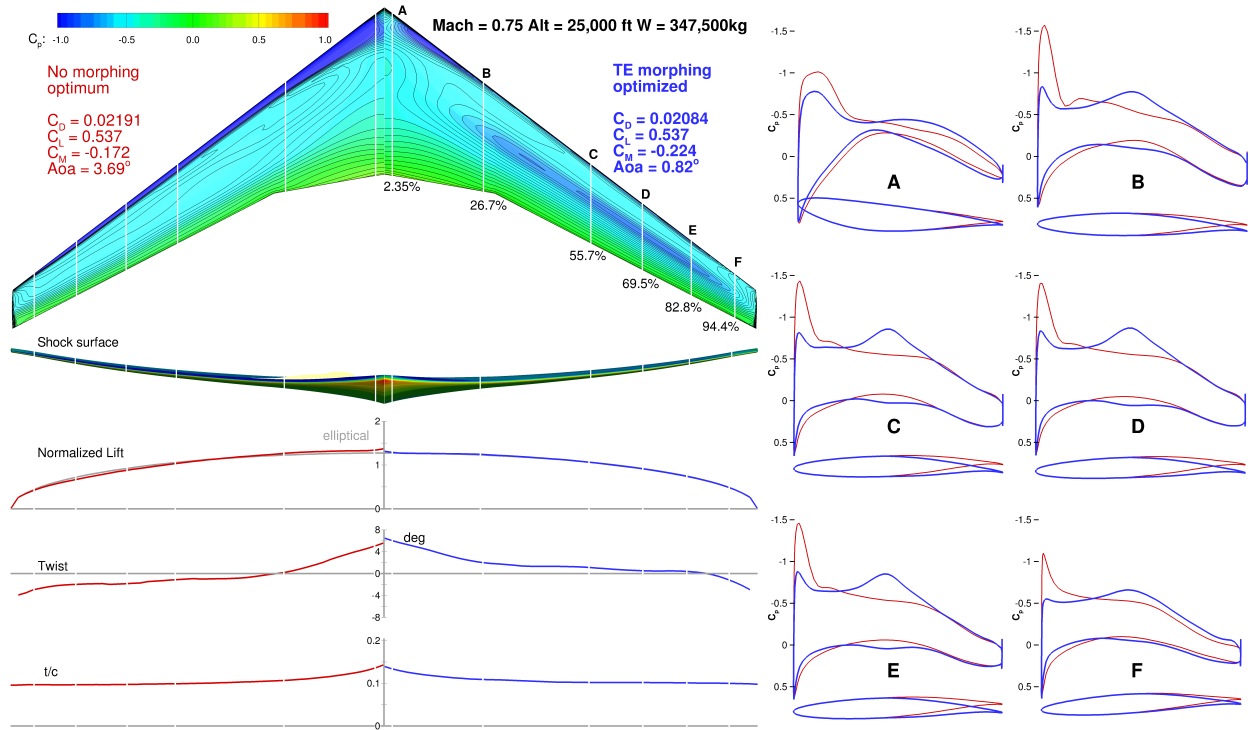


Figure 6: Morphing TE optimization at low-Mach low-altitude off-design condition.

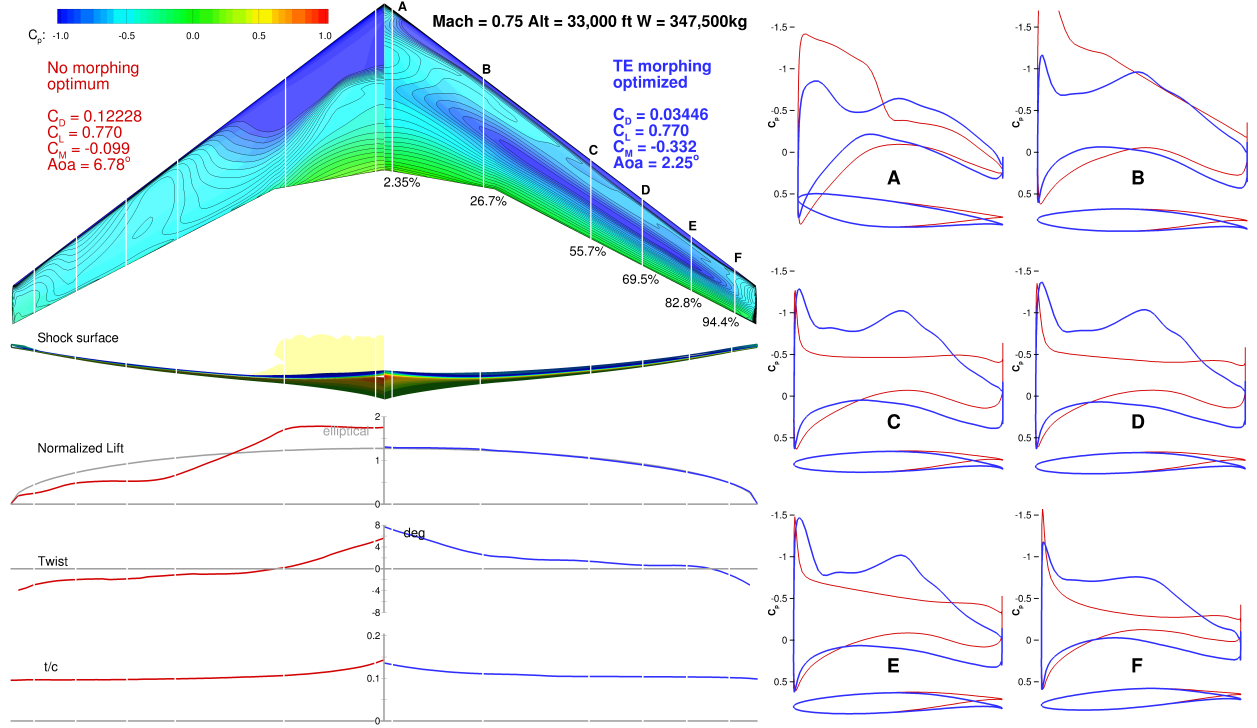


Figure 7: Morphing TE optimization at low-Mach high-altitude off-design condition.

high altitude and low Mach, where the lift coefficient is the highest. For high Mach numbers above 0.85, the trend reverses because of the drag divergence.

In Fig. 11 we plot the ML/D contours of the multipoint baseline, morphing TE, and fully morphing wing designs with respect to altitude and Mach number. The ML/D contours for the other weights are shown in Appendix C (Figs. 29 and 30). ML/D provides a metric for quantifying the aircraft range based on the Breguet range equation with constant thrust-specific fuel consumption. While the thrust-specific fuel consumption is actually not constant, assuming it to be constant is acceptable when comparing performance in a limited Mach number range [32]. We add 100 drag counts to the computed drag to account for the drag due to the fuselage, tail, and nacelles; this gives more realistic ML/D values. In aircraft design, the 99% value of the maximum ML/D contour, shown in black, is often used to examine the robustness of the design [23]. The point with the highest Mach number on that contour line corresponds to the LRC point, which is the point at which the aircraft can fly at a higher speed by incurring a 1% increase in fuel burn [33].

The multipoint baseline maximum ML/D occurs at the nominal flight condition (Mach 0.85; 31,000 ft altitude). Both the morphing TE and the morphing wing increase the maximum ML/D . The maximum ML/D points for the morphing TE and morphing wing are at a higher altitude and higher Mach number. Since the TE shape can be adapted for each flight condition, the drag divergence is pushed to a higher Mach number. The 99% value of the maximum ML/D contour of the morphing designs is also significantly enlarged, indicating a more robust design. We see that the morphing TE enables the aircraft to fly higher and faster without a fuel-burn penalty. To more accurately capture the tradeoffs, we would need to perform a multidisciplinary study including low-speed aerodynamics, propulsion, and structure.

8 Morphing Trailing Edge Mission Fuel-Burn Reduction

Since we have morphing TE optimizations spanning the entire flight envelope, we can create a surrogate model of optimal TE shapes for different flight conditions. This database allows us to compute the fuel burn for a series of missions without performing any additional optimizations. Since we have a relatively fine discretization of the flight region, we use a linear interpolation to evaluate the performance and optimal shape between the optimized points. A thrust-specific fuel consumption (TSFC) of 0.53 lb/(lbf · h) is assumed. We also add 100 drag counts to the computed drag to account for the drag due to the fuselage, tail, and nacelles. The fuel burn is then integrated backwards for a given flight profile. Figure 12 shows a typical

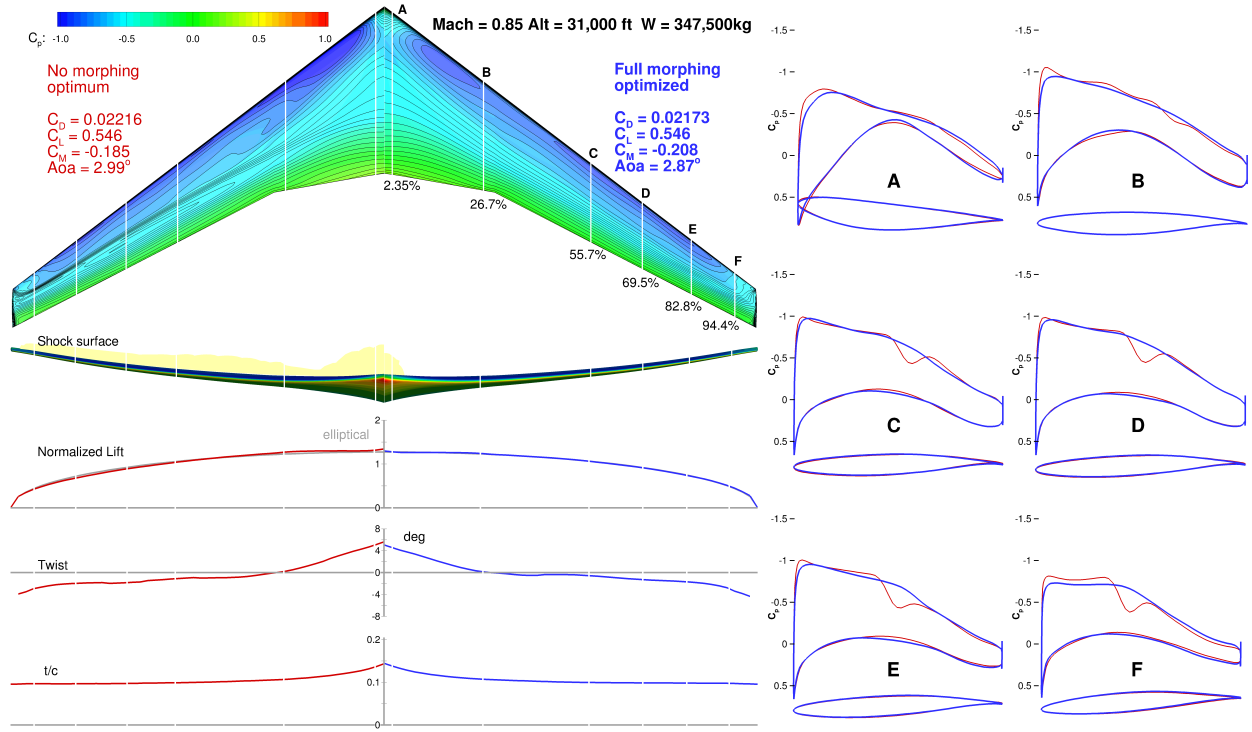


Figure 8: Fully morphing wing optimization at MTOW on-design condition.

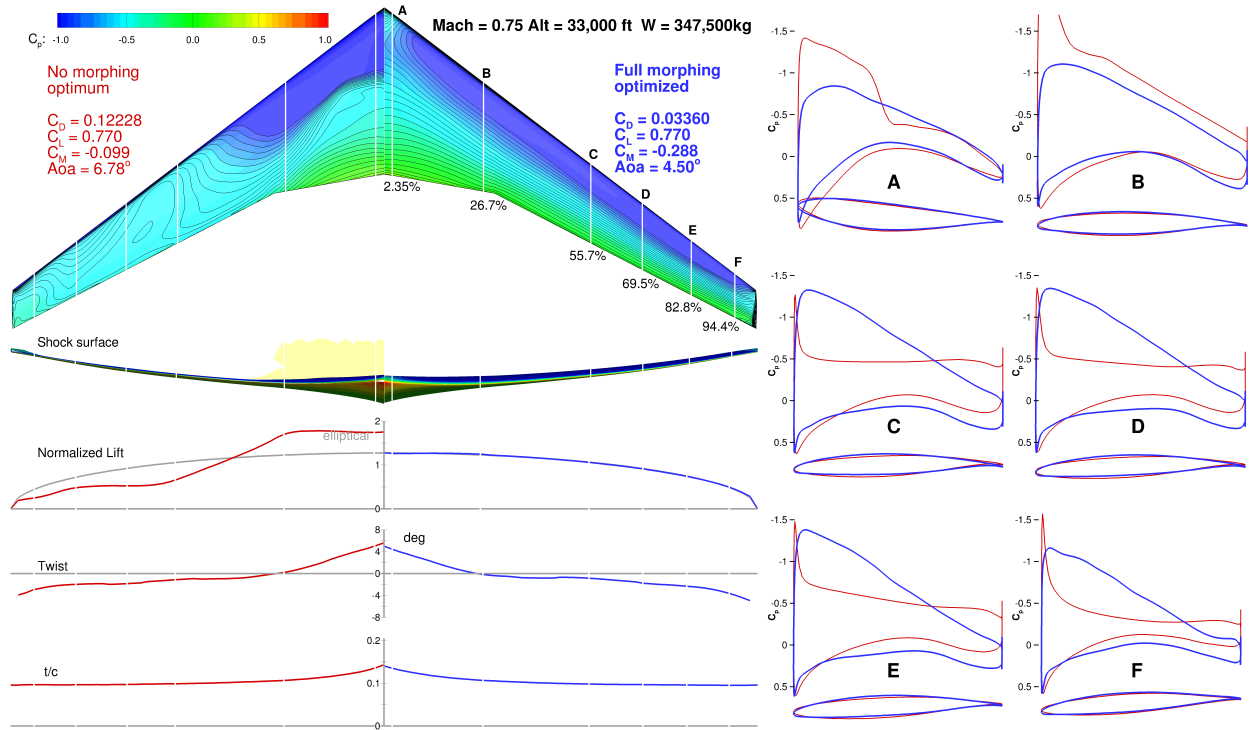
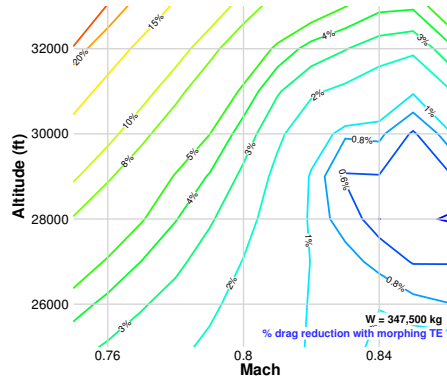
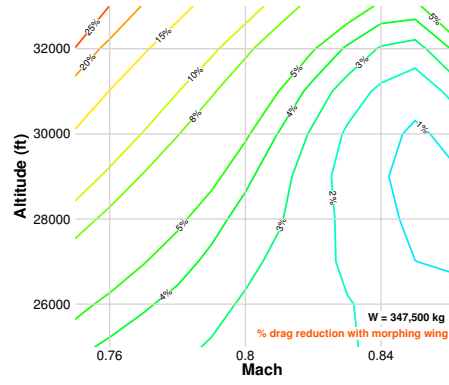


Figure 9: Fully morphing wing optimization at low-Mach high-altitude off-design condition.

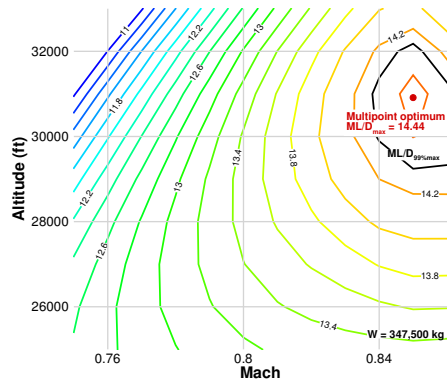


(a) Morphing TE

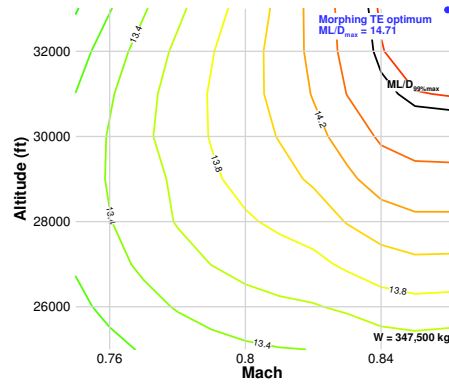


(b) Fully morphing wing

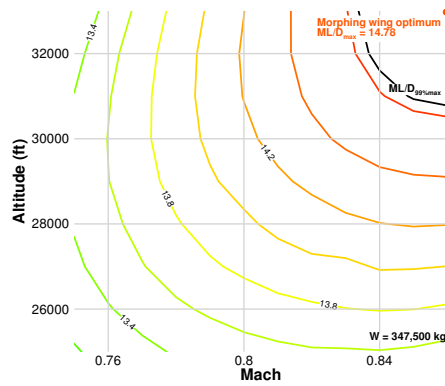
Figure 10: The trends of the drag reduction contours are similar, with a drag reduction of about 1% near on-design conditions.



(a) Multipoint optimized baseline



(b) Morphing TE wing



(c) Fully morphing wing

Figure 11: The maximum ML/D occurs at a higher altitude and Mach number with morphing

flight profile for a long-range flight (this flight from Dallas Fort Worth to Sydney, Australia is currently the longest nonstop commercial flight).

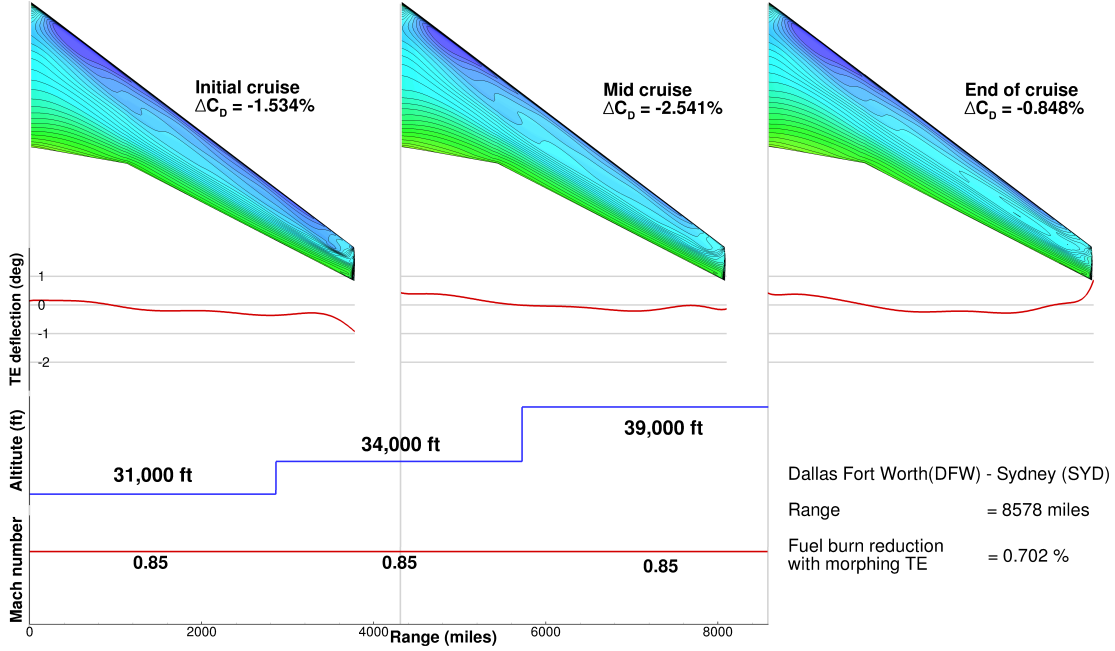


Figure 12: Fuel burn is reduced by 0.7% using morphing TE for DFW–SYD flight.

Since the flight is operated in the on-design condition with step climb, the TE deflection is within 1 degree. The wing tip exhibits the highest amount of deflection, from -1 degree at the initial cruise to 1 degree near the end of the cruise. We see a 0.7% fuel-burn reduction using morphing TE on this flight. As pointed out in Section 5, the morphing TE has higher drag reduction at off-design conditions. Table 4 shows the drag reduction for a number of hypothetical flight trajectories.

Route	Distance (mi)	Mach numbers	Cruise altitudes (ft)	Fuel-burn reduction
DFW–SYD	8578	0.85, 0.85, 0.85	31,000, 34,000, 39,000	-0.702%
DTW–PVG	7120	0.85, 0.85, 0.85	33,000, 36,000, 41,000	-1.023%
LAX–NRT	5440	0.80, 0.85, 0.80	33,000, 33,000, 33,000	-1.049%
JFK–SFO	2580	0.84, 0.84, 0.84	32,000, 34,000, 36,000	-1.207%
ATL–ORD	606	0.78, 0.80, 0.78	31,000, 31,000, 31,000	-1.074%
–	2000	0.75, 0.75, 0.75	29,000, 31,000, 34,000	-1.680%

Table 4: The fuel-burn reduction is about 1% using morphing TE for various flight trajectories.

We see that the morphing TE provides about 1% fuel-burn reduction at cruise condition for the simulated flights in Table 4. All of the simulated flights have a TE deflection within 2 degrees. Additional benefits could be realized during the climb and descent, which are neglected in this analysis. To evaluate the climb and descent, additional optimizations at lower speeds and lower altitudes would be needed to span the flight envelope for climb and descent.

9 Conclusions

We performed the aerodynamic shape optimization of a wide-body long-range aircraft wing (based on the NASA CRM model) with an adaptive morphing TE. For comparison, we started with a multipoint optimized baseline wing with no morphing, which served as the starting point for the morphing designs. We performed a total of 407 TE optimizations with different Mach numbers, altitudes, and weights to span the entire cruise flight envelope. We also optimized a morphing wing that assumed complete freedom in shape. The results

Wing configuration	Mach	Altitude (ft)	C_L	C_D	ΔC_D (%)
CRM	0.85	34,000	0.50	0.02115	+6.1%
Baseline	0.85	34,000	0.50	0.01994	0.0%
	0.85	31,000	0.43	0.01718	0.0%
	0.75	25,000	0.54	0.02191	0.0%
Morphing TE	0.85	31,000	0.43	0.01693	-1.5%
	0.75	25,000	0.54	0.02084	-4.9%
Fully morphing	0.85	31,000	0.43	0.01679	-2.3%
	0.75	25,000	0.54	0.02056	-6.2%

Table 5: Summary of performance for the original CRM wing, the multipoint optimized baseline, the optimized morphing TE, and the optimized fully morphing wings.

are summarized in Table 5.

For the morphing TE wing, a drag reduction of the order of 1% was achieved for on-design conditions, and reductions up to 5% were achieved for off-design conditions. We further evaluated the performance of the morphing TE by comparing its benefits with those from a fully morphing wing. We did this by plotting the drag reduction contour and the ML/D contour. The fully morphing wing yielded only marginally lower drag and a similar ML/D contour. Therefore, morphing only the TE can achieve an aerodynamic performance similar to that of a fully morphing wing without the drastic increase in wing morphing mechanism and weight.

Finally, we created a surrogate model of optimal TE shapes to compute the cruise fuel burn for different flight missions. We observed about 1% fuel-burn reduction using the morphing TE. More significant fuel-burn reduction could be achieved in the climb and descent segments.

From an aerodynamic perspective, an adaptive morphing TE can easily offer additional drag reduction without a complete redesign of the wing. Since this technology has been demonstrated by FlexSys, and could be installed on conventional control surfaces, we could consider retrofitting existing aircraft. To thoroughly evaluate the benefits, it will be necessary to perform a multidisciplinary study to examine the tradeoffs between aerodynamics, structures, and controls. This study should include planform design variables, since the load alleviation due to morphing will allow for larger spans with little or no weight penalty. We have already performed a preliminary aerostructural optimization study [34].

10 Acknowledgments

The computations were performed on the Flux HPC cluster at the University of Michigan Center of Advanced Computing, and on the Gordon cluster of the Extreme Science and Engineering Discovery Environment (XSEDE), which is supported by National Science Foundation grant number ACI-1053575. This research is partially funded by FlexSys, Inc. The authors would like to thank Yin Yu for his assistance in generating some of the figures, and we are grateful to our MDOLab colleagues for their suggestions.

References

- [1] Kota, S., Hetrick, J., Osborn, R., Paul, D., Pendleton, E., Flick, P., and Tilmann, C., “Design and Application of Compliant Mechanisms for Morphing Aircraft Structures,” *Proceedings of the SPIE Smart Structures and Materials Conference*, San Diego, CA, March 2003.
- [2] Kota, S., Osborn, R., Ervin, G., Maric, D., Flick, P., and Paul, D., “Mission Adaptive Compliant Wing—Design, Fabrication and Flight Test,” *RTO Applied Vehicle Technology Panel (AVT) Symposium*, 2009.
- [3] Sofa, A. Y. N., Meguid, S. A., Tan, K. T., and Yeo, W. K., “Shape Morphing of Aircraft Wing: Status and Challenges,” *Materials & Design*, Vol. 31, No. 3, 3 2010, pp. 1284–1292. doi:10.1016/j.matdes.2009.09.011.

- [4] Molinari, G., Quack, M., Dmitriev, V., Morari, M., Jenny, P., and Ermanni, P., “Aero-Structural Optimization of Morphing Airfoils for Adaptive Wings,” *Journal of Intelligent Material Systems and Structures*, Vol. 22, No. 10, 2011, pp. 1075–1089. doi:[10.1177/1045389X11414089](https://doi.org/10.1177/1045389X11414089).
- [5] Lee, D., Gonzalez, L. F., Periaux, J., and Onate, E., “Robust Aerodynamic Design Optimisation of Morphing Aerofoil/Wing using Distributed MOGA,” *Proceedings of the 28th Congress of the International Council of the Aeronautical Sciences*, Optimage Ltd., on behalf of the International Council of the Aeronautical Sciences (ICAS), 2012.
- [6] Lyu, Z., Kenway, G. K., Paige, C., and Martins, J. R. R. A., “Automatic Differentiation Adjoint of the Reynolds-Averaged Navier–Stokes Equations with a Turbulence Model,” *21st AIAA Computational Fluid Dynamics Conference*, San Diego, CA, Jul. 2013. doi:[10.2514/6.2013-2581](https://doi.org/10.2514/6.2013-2581).
- [7] Kenway, G. K. W., Kennedy, G. J., and Martins, J. R. R. A., “Scalable Parallel Approach for High-Fidelity Steady-State Aeroelastic Analysis and Derivative Computations,” *AIAA Journal*, Vol. 52, No. 5, May 2014, pp. 935–951. doi:[10.2514/1.J052255](https://doi.org/10.2514/1.J052255).
- [8] Kenway, G. K. W. and Martins, J. R. R. A., “Multipoint High-Fidelity Aerostructural Optimization of a Transport Aircraft Configuration,” *Journal of Aircraft*, Vol. 51, No. 1, January 2014, pp. 144–160. doi:[10.2514/1.C032150](https://doi.org/10.2514/1.C032150).
- [9] Lyu, Z. and Martins, J. R. R. A., “Aerodynamic Design Optimization Studies of a Blended-Wing-Body Aircraft,” *Journal of Aircraft*, Vol. 51, No. 5, September 2014, pp. 1604–1617. doi:[10.2514/1.C032491](https://doi.org/10.2514/1.C032491).
- [10] Lyu, Z., Kenway, G. K., and Martins, J. R. R. A., “Aerodynamic Shape Optimization Studies on the Common Research Model Wing Benchmark,” *AIAA Journal*, Vol. 53, No. 4, April 2015, pp. 968–985. doi:[10.2514/1.J053318](https://doi.org/10.2514/1.J053318).
- [11] Lyu, Z. and Martins, J. R. R. A., “Strategies for Solving High-Fidelity Aerodynamic Shape Optimization Problems,” *15th AIAA/ISSMO Multidisciplinary Analysis and Optimization Conference*, Atlanta, GA, June 2014. doi:[10.2514/6.2014-2594](https://doi.org/10.2514/6.2014-2594), AIAA 2014-2594.
- [12] Lyu, Z., Xu, Z., and Martins, J. R. R. A., “Benchmarking Optimization Algorithms for Wing Aerodynamic Design Optimization,” *Proceedings of the 8th International Conference on Computational Fluid Dynamics*, Chengdu, Sichuan, China, July 2014, ICCFD8-2014-0203.
- [13] Kenway, G. K., Kennedy, G. J., and Martins, J. R. R. A., “A CAD-Free Approach to High-Fidelity Aerostructural Optimization,” *Proceedings of the 13th AIAA/ISSMO Multidisciplinary Analysis Optimization Conference*, Fort Worth, TX, Sept. 2010, AIAA 2010-9231.
- [14] van der Weide, E., Kalitzin, G., Schluter, J., and Alonso, J. J., “Unsteady Turbomachinery Computations Using Massively Parallel Platforms,” *Proceedings of the 44th AIAA Aerospace Sciences Meeting and Exhibit*, Reno, NV, 2006, AIAA 2006-0421.
- [15] Jameson, A., Schmidt, W., and Turkel, E., “Numerical Solution of the Euler Equations by Finite Volume Methods Using Runge-Kutta Time Stepping Schemes,” *AIAA Paper* 81-1259, 1981.
- [16] Mader, C. A., Martins, J. R. R. A., Alonso, J. J., and van der Weide, E., “ADjoint: An Approach for the Rapid Development of Discrete Adjoint Solvers,” *AIAA Journal*, Vol. 46, No. 4, April 2008, pp. 863–873. doi:[10.2514/1.29123](https://doi.org/10.2514/1.29123).
- [17] Saad, Y. and Schultz, M. H., “GMRES: A Generalized Minimal Residual Algorithm for Solving Non-symmetric Linear Systems,” *SIAM Journal on Scientific and Statistical Computing*, Vol. 7, No. 3, 1986, pp. 856–869. doi:[10.1137/0907058](https://doi.org/10.1137/0907058).
- [18] Balay, S., Gropp, W. D., McInnes, L. C., and Smith, B. F., *Efficient Management of Parallelism in Object Oriented Numerical Software Libraries*, Birkhäuser Press, 1997, pp. 163–202.

- [19] Balay, S., Brown, J., Buschelman, K., Eijkhout, V., Gropp, W. D., Kaushik, D., Knepley, M. G., McInnes, L. C., Smith, B. F., and Zhang, H., “PETSc Users Manual,” Tech. Rep. ANL-95/11 - Revision 3.4, Argonne National Laboratory, 2013.
- [20] Balay, S., Brown, J., Buschelman, K., Gropp, W. D., Kaushik, D., Knepley, M. G., McInnes, L. C., Smith, B. F., and Zhang, H., “PETSc Web page,” 2013, <http://www.mcs.anl.gov/petsc>.
- [21] Gill, P. E., Murray, W., and Saunders, M. A., “SNOPT: An SQP algorithm for large-scale constrained optimization,” *SIAM Journal of Optimization*, Vol. 12, No. 4, 2002, pp. 979–1006. doi:[10.1137/S1052623499350013](https://doi.org/10.1137/S1052623499350013).
- [22] Perez, R. E., Jansen, P. W., and Martins, J. R. R. A., “pyOpt: A Python-Based Object-Oriented Framework for Nonlinear Constrained Optimization,” *Structural and Multidisciplinary Optimization*, Vol. 45, No. 1, January 2012, pp. 101–118. doi:[10.1007/s00158-011-0666-3](https://doi.org/10.1007/s00158-011-0666-3).
- [23] Vassberg, J. C., DeHaan, M. A., Rivers, S. M., and Wahls, R. A., “Development of a Common Research Model for Applied CFD Validation Studies,” 2008, AIAA 2008-6919.
- [24] Vassberg, J., “A Unified Baseline Grid about the Common Research Model Wing/Body for the Fifth AIAA CFD Drag Prediction Workshop (Invited),” *29th AIAA Applied Aerodynamics Conference*, Jul 2011. doi:[10.2514/6.2011-3508](https://doi.org/10.2514/6.2011-3508).
- [25] Roache, P. J., “Verification of Codes and Calculations,” *AIAA Journal*, Vol. 36, No. 5, 1998, pp. 696–702. doi:[10.2514/2.457](https://doi.org/10.2514/2.457).
- [26] Kenway, G. K. W. and Martins, J. R. R. A., “Multipoint Aerodynamic Shape Optimization Investigations of the Common Research Model Wing,” *AIAA Journal*, 2015. doi:[10.2514/1.J054154](https://doi.org/10.2514/1.J054154), (In press).
- [27] Liem, R., Kenway, G. K. W., and Martins, J. R. R. A., “Multimission Aircraft Fuel Burn Minimization via Multipoint Aerostructural Optimization,” *AIAA Journal*, Vol. 53, No. 1, January 2015, pp. 104–122. doi:[10.2514/1.J052940](https://doi.org/10.2514/1.J052940).
- [28] Haimes, R., “Automated Feature Extraction from Transient CFD Simulations,” *Proceeding of the 7th Annual Conference of the CFD Society of Canada, Halifax, NS*, May 1999.
- [29] Vassberg, J. and Jameson, A., “Influence of Shape Parameterization on Aerodynamic Shape Optimization,” Tech. rep., Von Karman Institute, Brussels, Belgium, April 2014.
- [30] Joo, J. J., Marks, C. R., Zientarski, L., and Culler, A. J., “Variable Camber Compliant Wing - Design,” *23rd AIAA/AHS Adaptive Structures Conference*, American Institute of Aeronautics and Astronautics (AIAA), jan 2015. doi:[10.2514/6.2015-1050](https://doi.org/10.2514/6.2015-1050).
- [31] Marks, C. R., Zientarski, L., Culler, A. J., Hagen, B., Smyers, B. M., and Joo, J. J., “Variable Camber Compliant Wing - Wind Tunnel Testing,” *23rd AIAA/AHS Adaptive Structures Conference*, American Institute of Aeronautics and Astronautics (AIAA), jan 2015. doi:[10.2514/6.2015-1051](https://doi.org/10.2514/6.2015-1051).
- [32] Torenbeek, E., *Advanced Aircraft Design: Conceptual Design, Analysis and Optimization of Subsonic Civil Airplanes*, Wiley, West Sussex, UK, 2013.
- [33] Roberson, W., Root, R., and Adams, D., “Fuel Conservation Strategies: Cruise Flight,” Tech. rep., Boeing AERO Magazine, 2007.
- [34] Burdette, D., Kenway, G. K. W., Lyu, Z., and Martins, J. R. R. A., “Aerostructural Design Optimization of an Adaptive Morphing Trailing Edge Wing,” *Proceedings of the AIAA Science and Technology Forum and Exposition (SciTech)*, Kissimmee, FL, January 2015, AIAA 2015-1129.

Appendix A: Morphing TE Optimization Results for Additional Flight Conditions

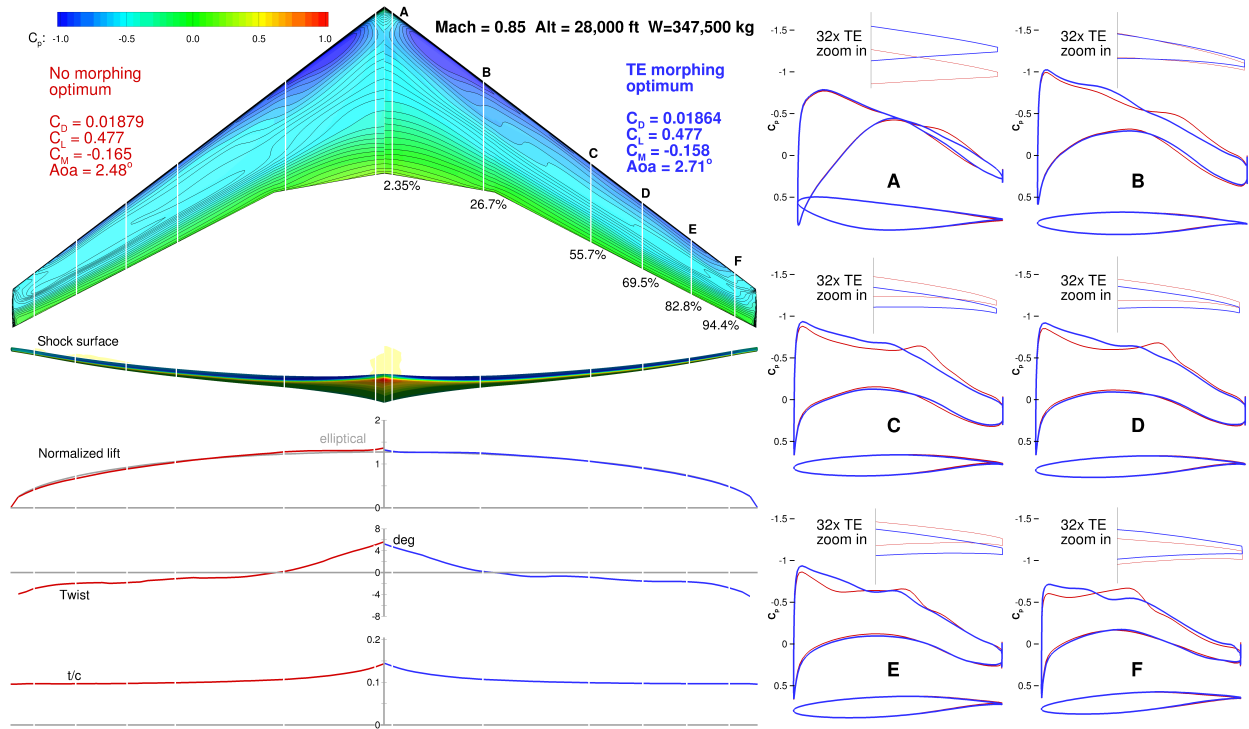


Figure 13: Morphing TE optimization at M = 0.85, Alt = 28,000 ft, and W = 347,500 kg.

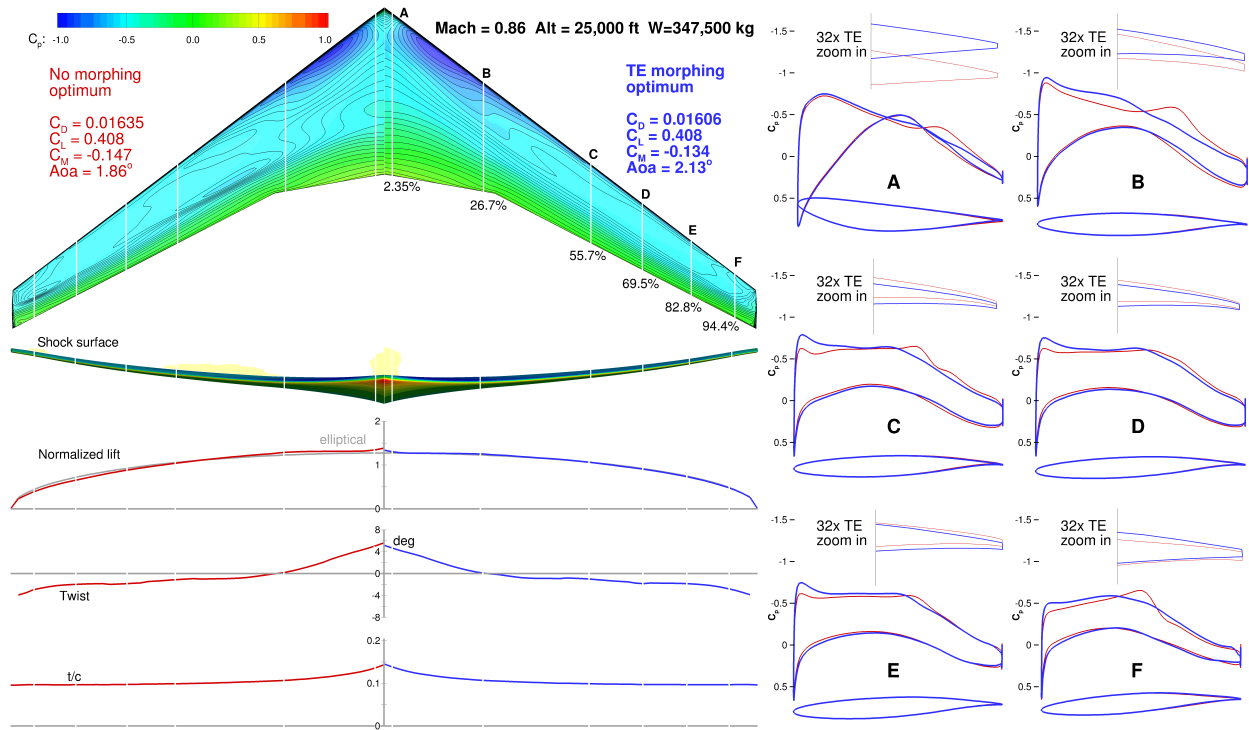


Figure 14: Morphing TE optimization at M = 0.86, Alt = 25,000 ft, and W = 347,500 kg.

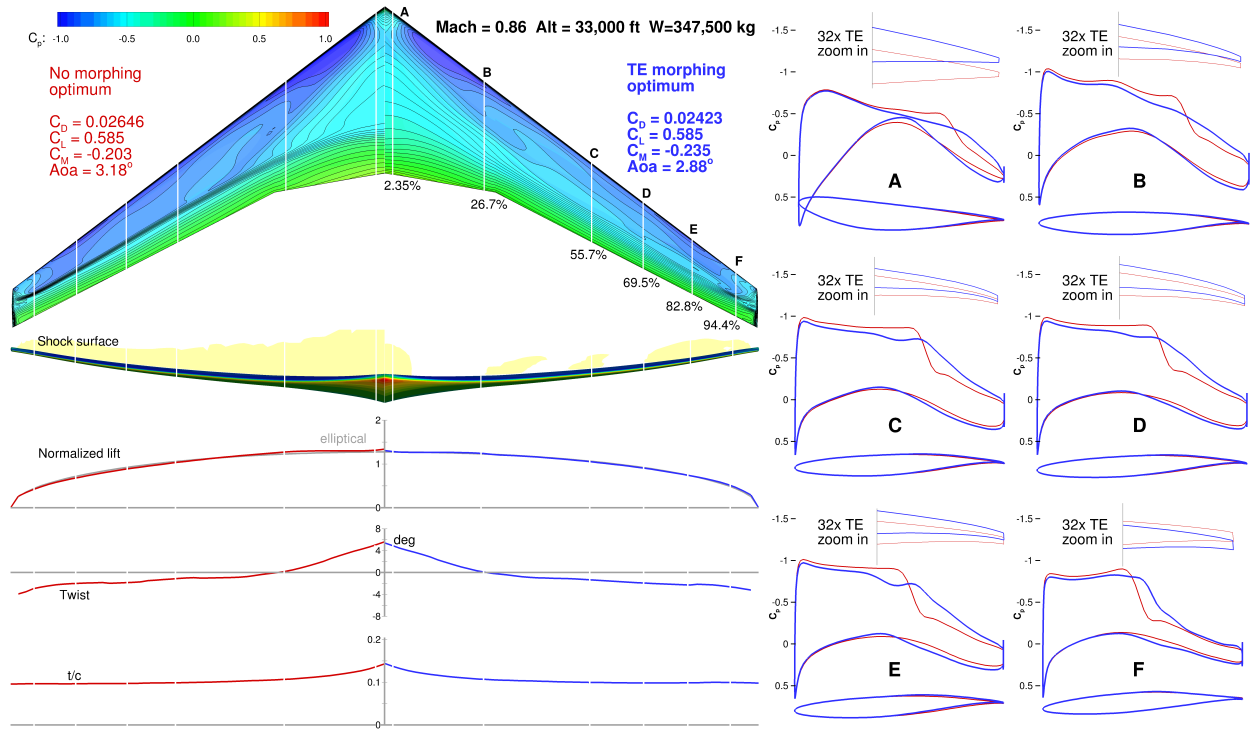


Figure 15: Morphing TE optimization at M = 0.86, Alt = 33,000 ft, and W = 347,500 kg.

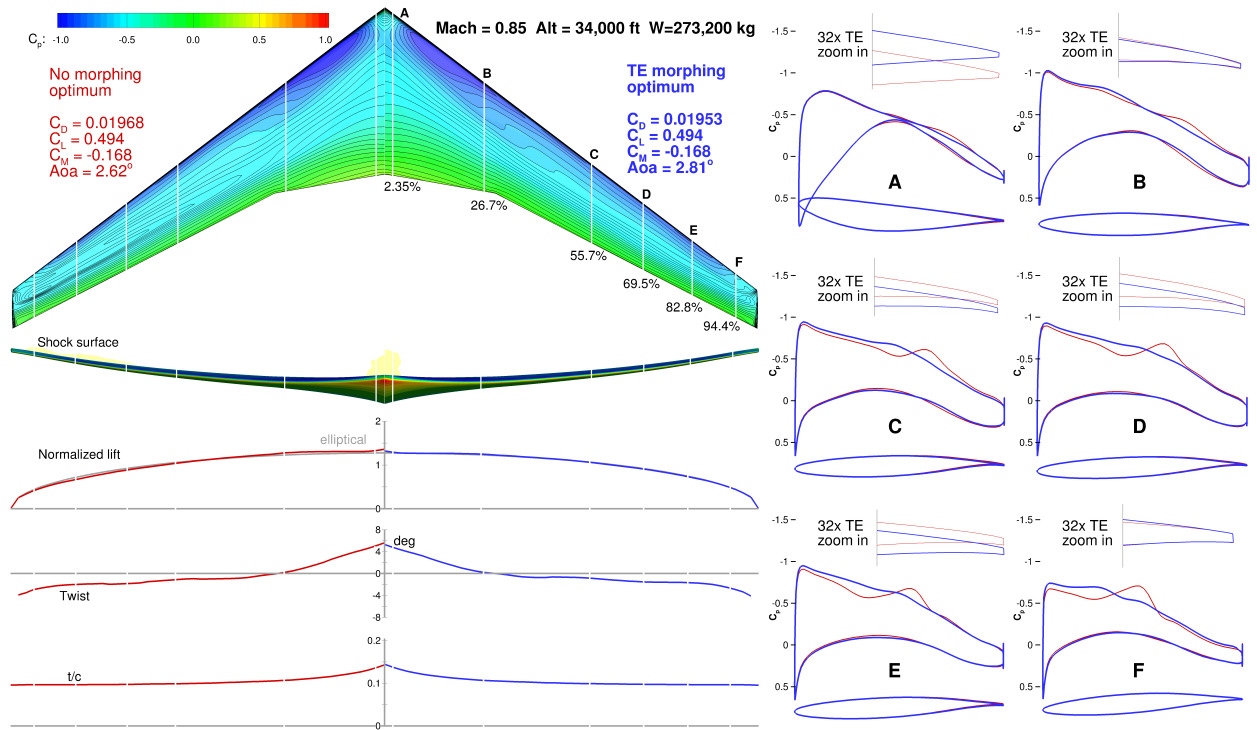


Figure 16: Morphing TE optimization at M = 0.85, Alt = 34,000 ft, and W = 273,200 kg.

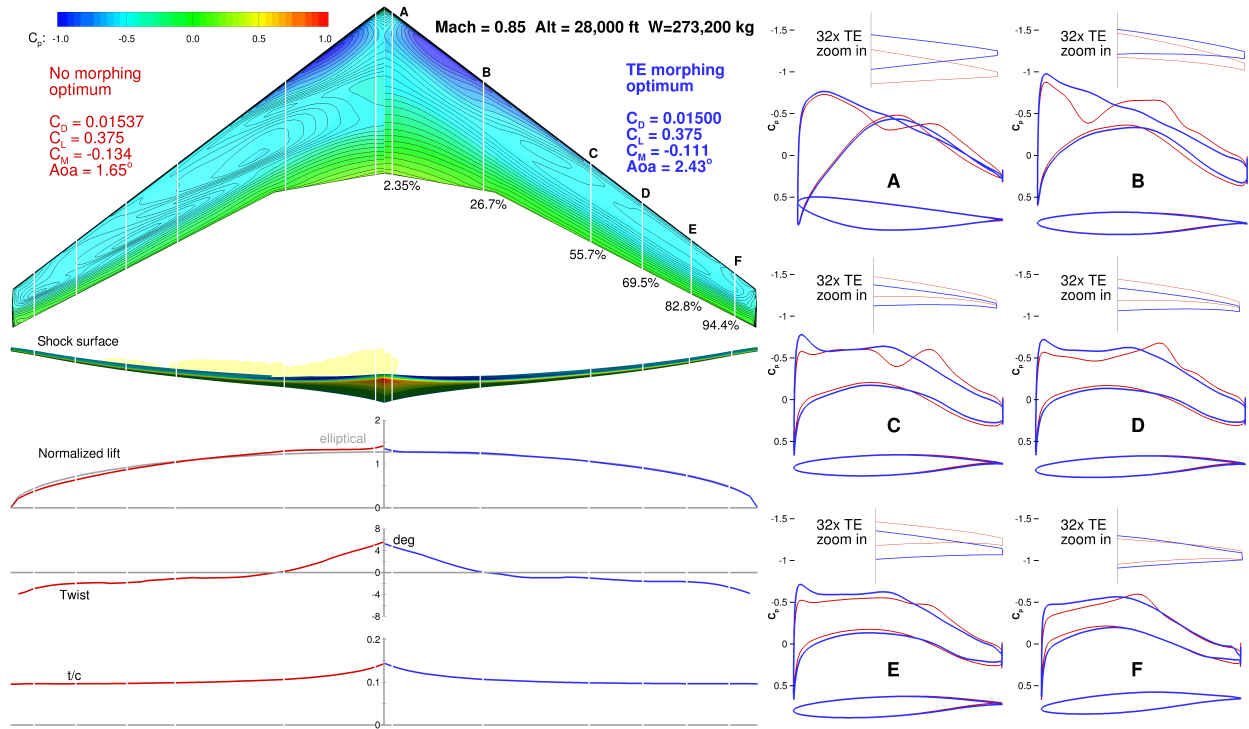


Figure 17: Morphing TE optimization at M = 0.85, Alt = 28,000 ft, and W = 273,200 kg.

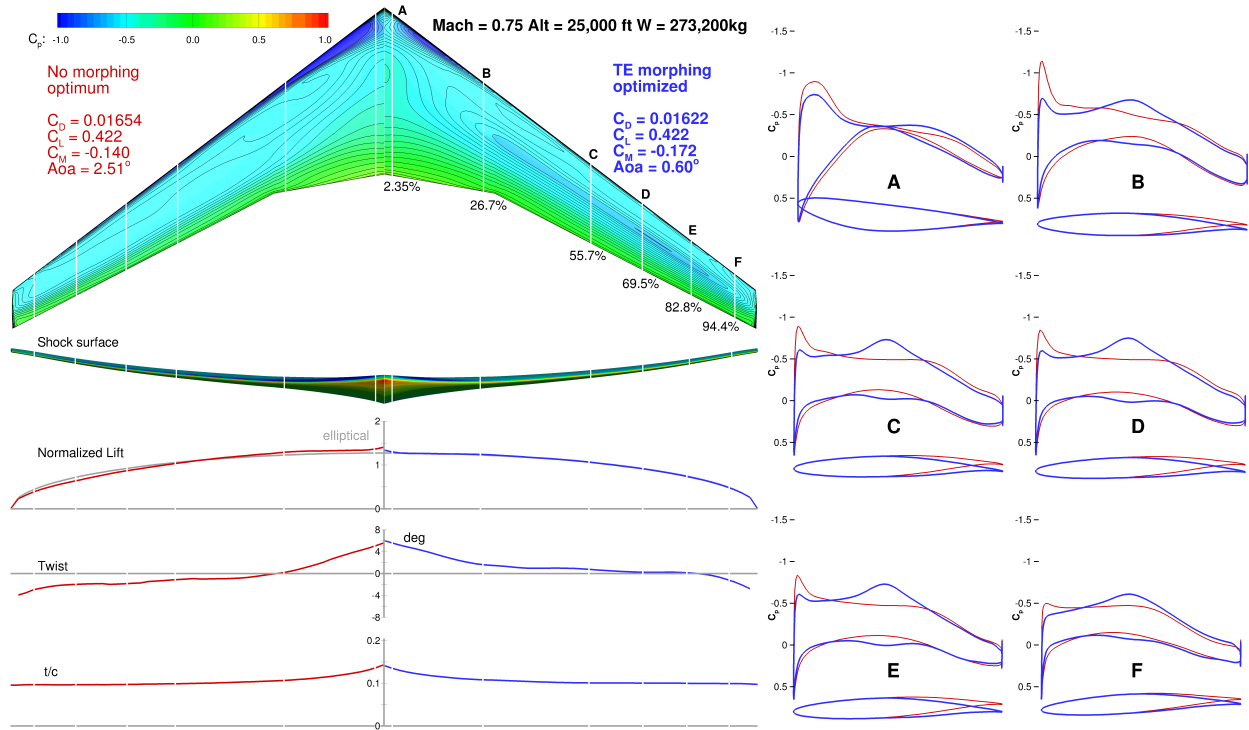


Figure 18: Morphing TE optimization at M = 0.75, Alt = 25,000 ft, and W = 273,200 kg.

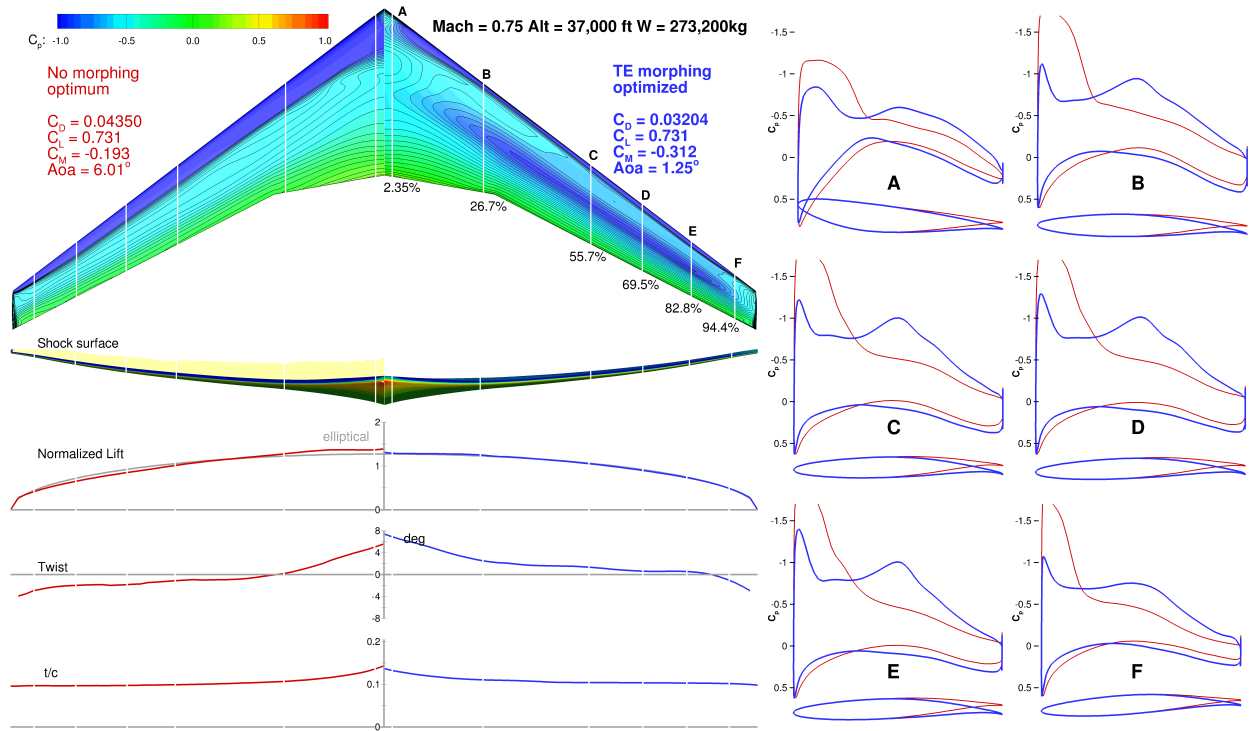


Figure 19: Morphing TE optimization at M = 0.75, Alt = 37,000 ft, and W = 273,200 kg.

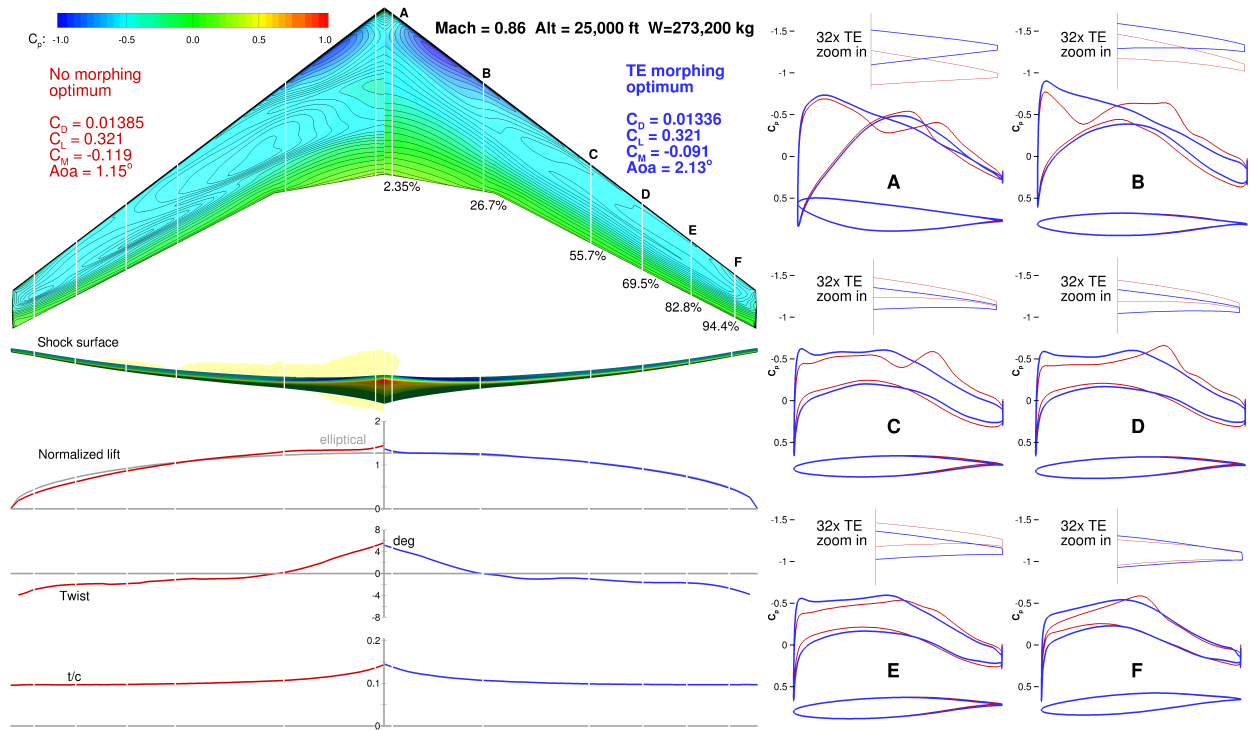


Figure 20: Morphing TE optimization at M = 0.86, Alt = 25,000 ft, and W = 273,200 kg.

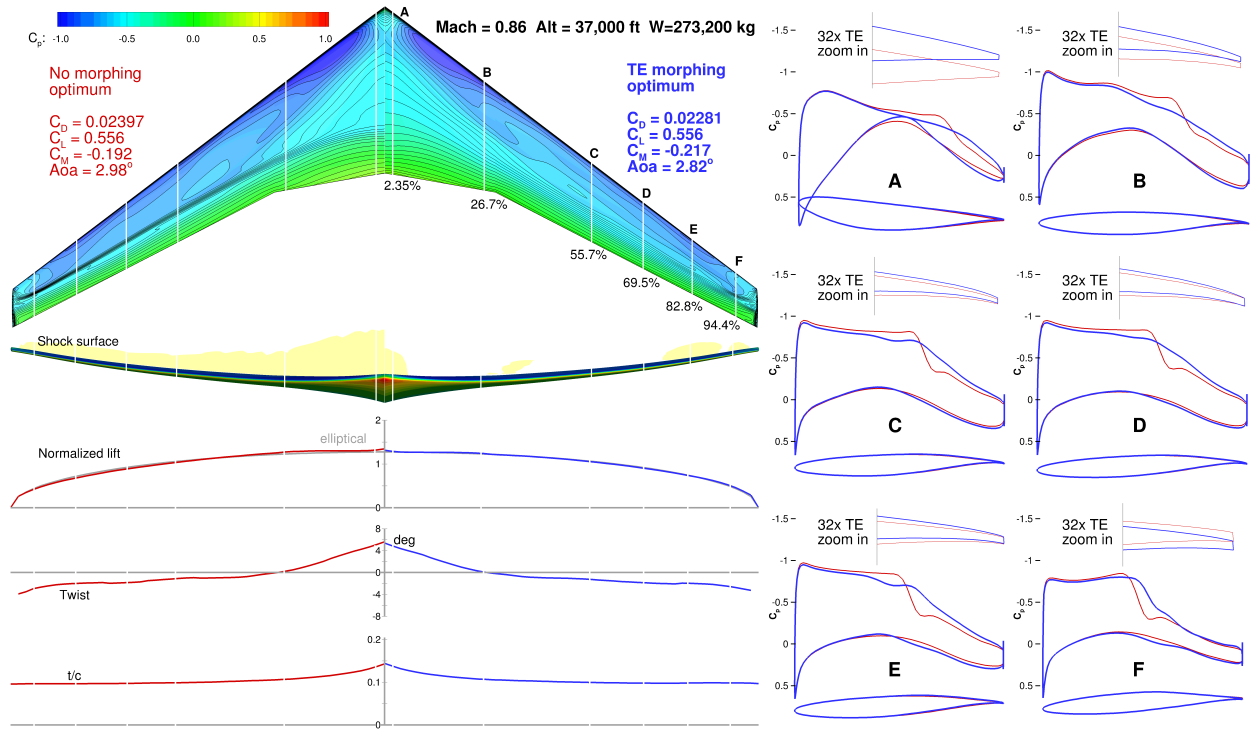


Figure 21: Morphing TE optimization at $M = 0.86$, Alt = 37,000 ft, and $W = 273,200$ kg.

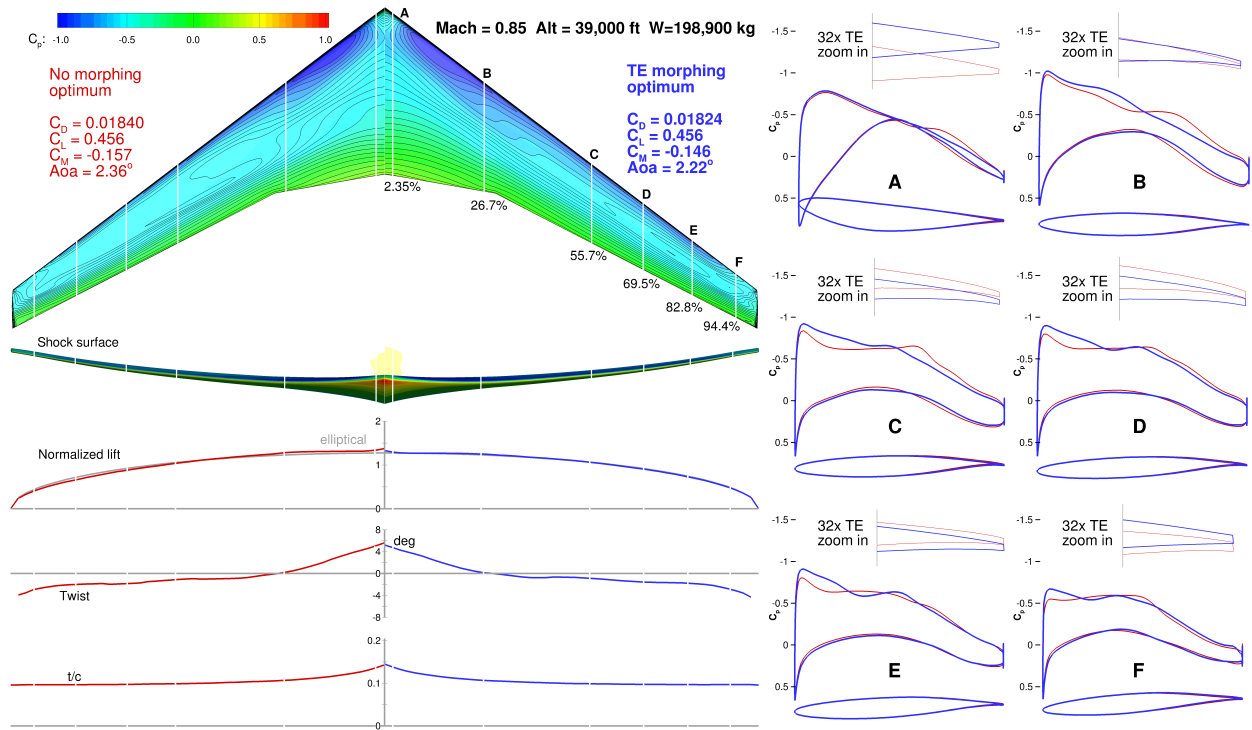


Figure 22: Morphing TE optimization at $M = 0.85$, Alt = 39,000 ft, and $W = 198,900$ kg.

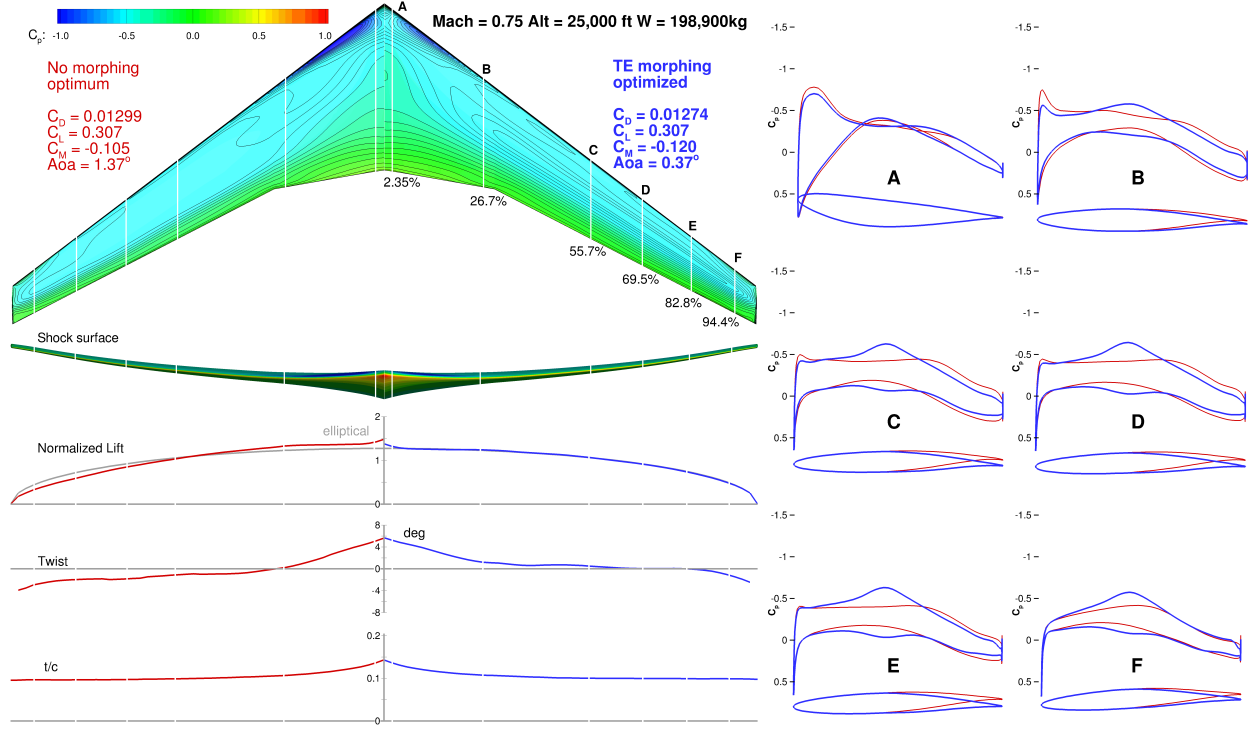


Figure 23: Morphing TE optimization at $M = 0.75$, Alt = 25,000 ft, and $W = 198,900$ kg.

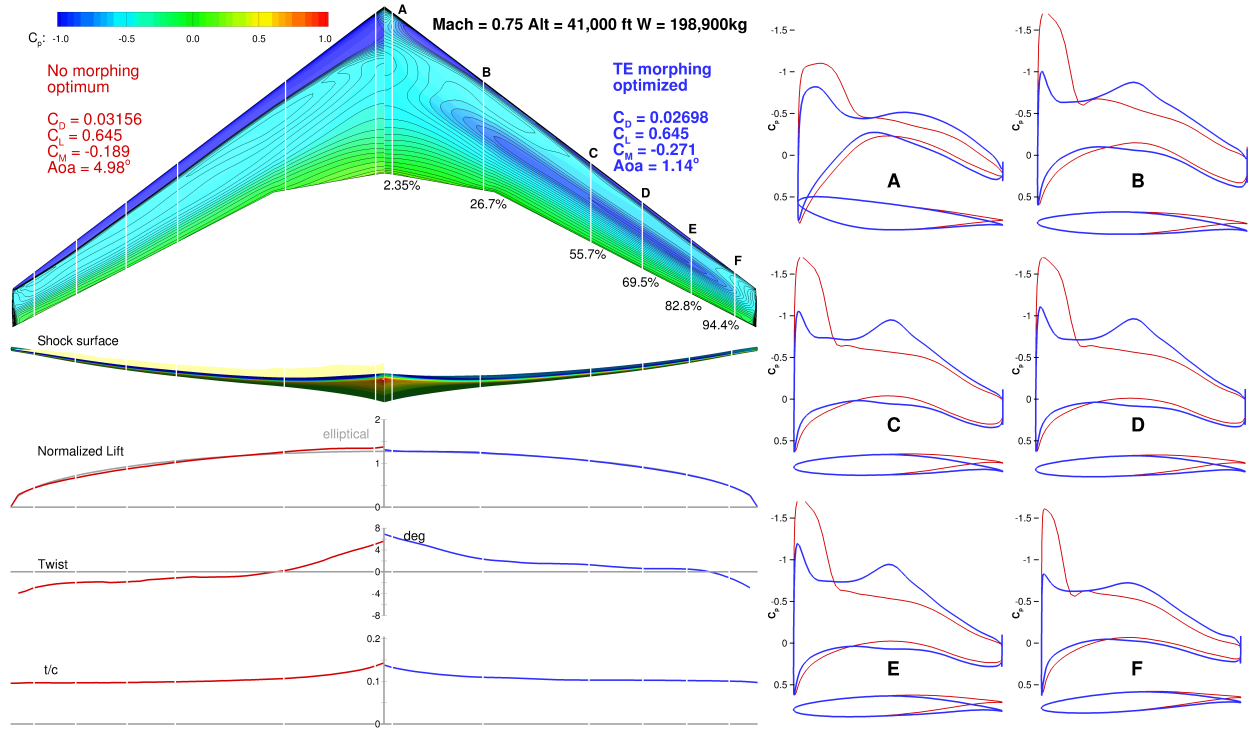


Figure 24: Morphing TE optimization at $M = 0.75$, Alt = 41,000 ft, and $W = 198,900$ kg.

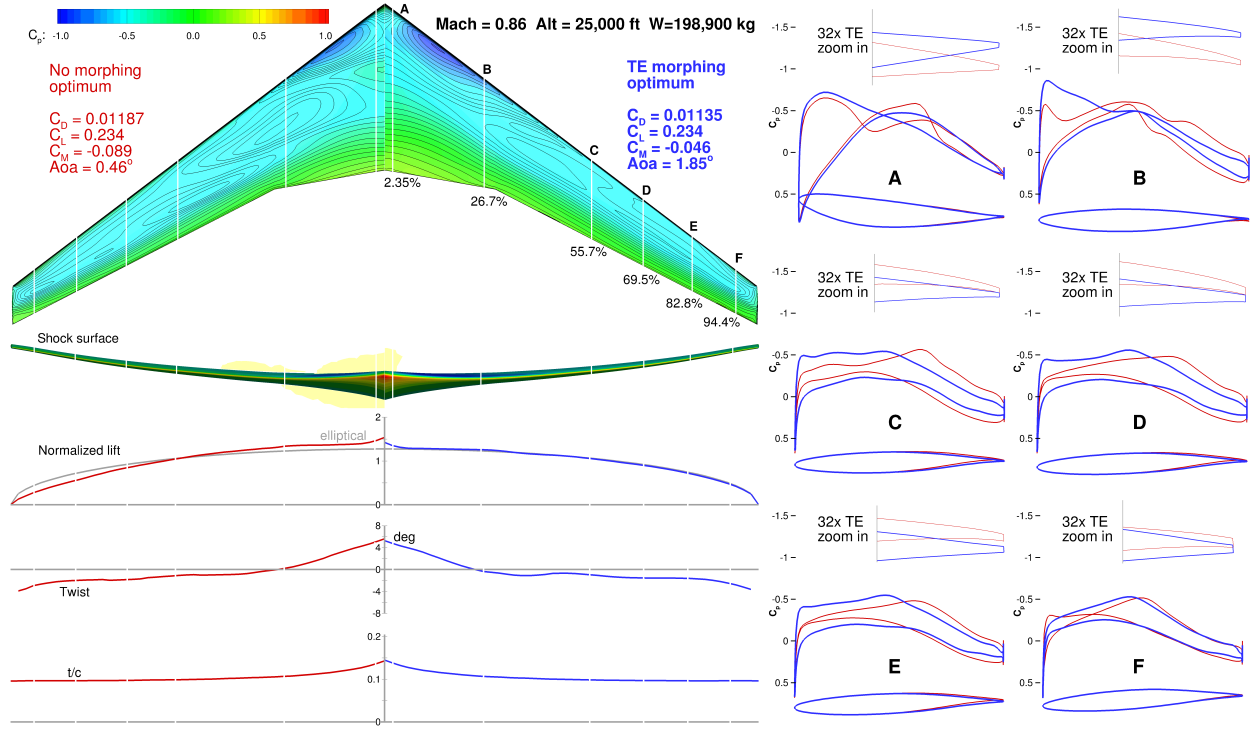


Figure 25: Morphing TE optimization at $M = 0.86$, Alt = 25,000 ft, and $W = 198,900$ kg.

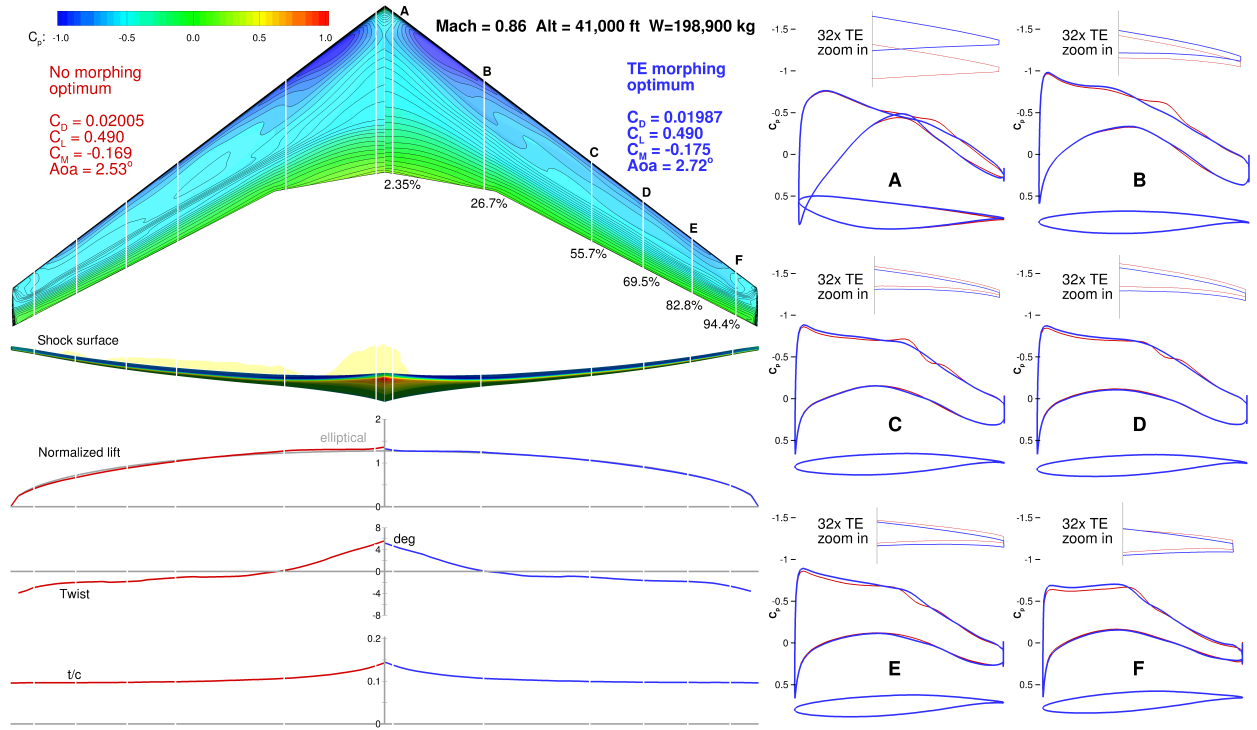
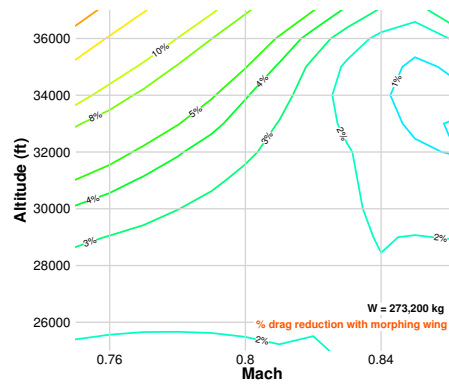
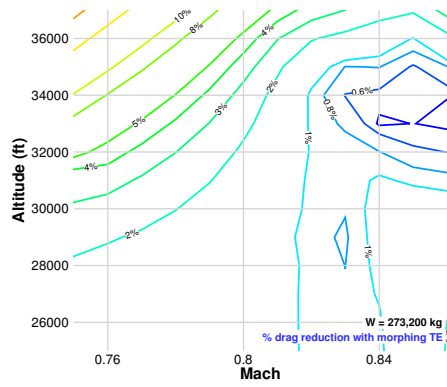
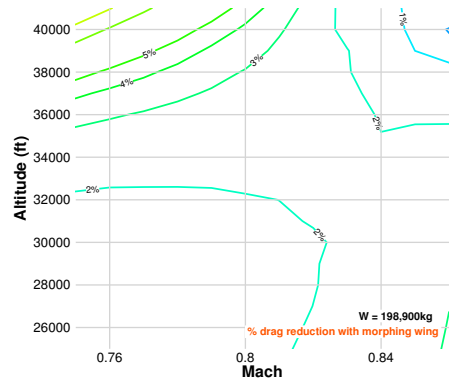
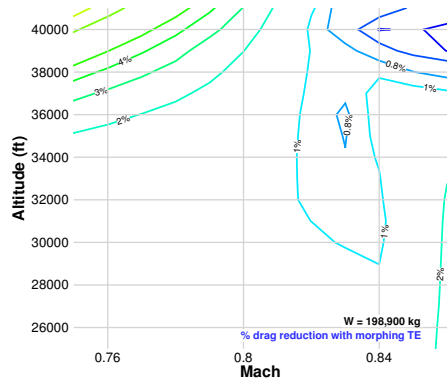


Figure 26: Morphing TE optimization at $M = 0.86$, Alt = 41,000 ft, and $W = 198,900$ kg.

Appendix B: Additional Drag Reduction Contours

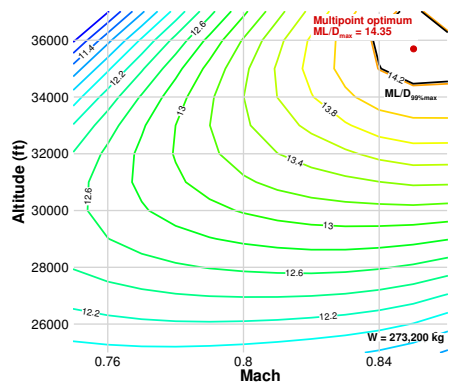


(a) Morphing TE (b) Morphing Wing
Figure 27: Drag reduction contour for $W = 273,200$ kg.

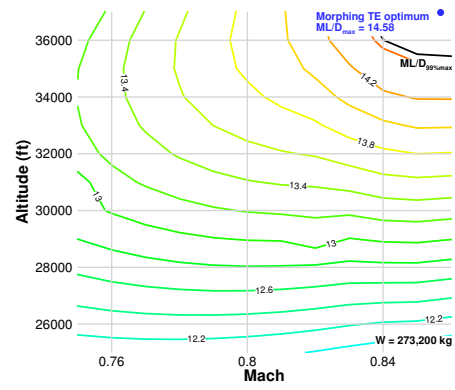


(a) Morphing TE (b) Morphing Wing
Figure 28: Drag reduction contour for $W = 198,900$ kg.

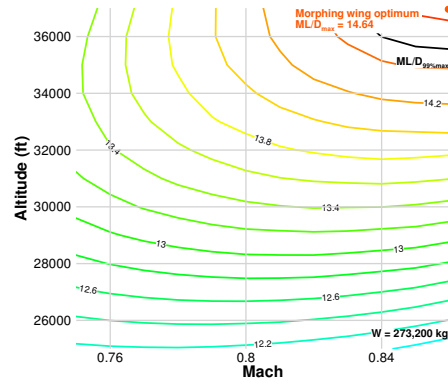
Appendix C: Additional ML/D Contours



(a) Multipoint optimized baseline

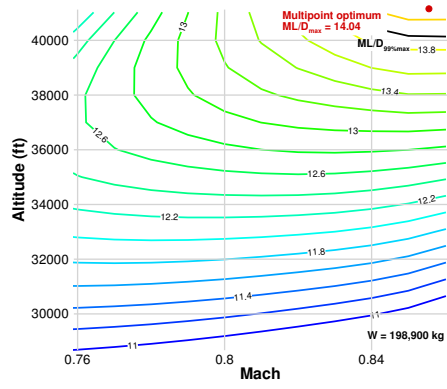


(b) Morphing TE

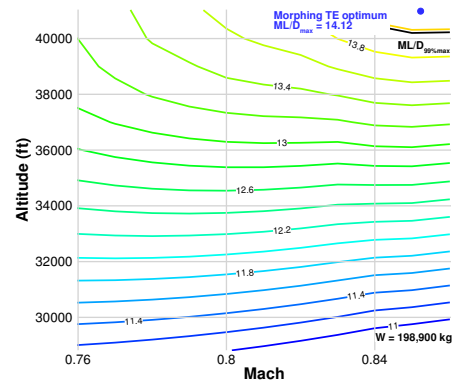


(c) Morphing Wing

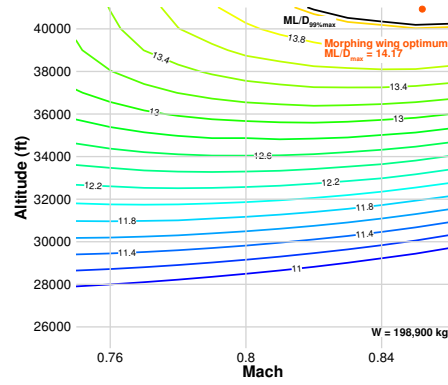
Figure 29: ML/D contour for $W = 273,200$ kg.



(a) Multipoint optimized baseline



(b) Morphing TE



(c) Morphing Wing

Figure 30: ML/D contour for $W = 198,900$ kg.